GROWTH AND CHARACTERIZATION OF LOW STRESS AMORPHOUS CARBON FILMS BY PULSED LASER DEPOSITION PROCESS

By

SANG HYUN YOON

A DISSERTATION PRESENTED TO THE GRADUATE SCHOOL
OF THE UNIVERSITY OF FLORIDA IN PARTIAL FULFILLMENT
OF THE REQUIREMENTS FOR THE DEGREE OF
DOCTOR OF PHILOSOPHY

UNIVERSITY OF FLORIDA

2004

Copyright 2004

by

Sang Hyun Yoon

To God, My Family & Puppies.

ACKNOWLEDGMENTS

I would like to express my sincere appreciation to my advisor, Dr. Rajiv K. Singh for his guidance, support, and encouragement. Thanks are also due to my doctoral committee members, Dr. Stephen J. Pearton, Dr. Cammy Abernathy, Dr. Wolfgang Sigmund, and Dr. Arthur F. Hebard, for their assistance and interest in my work.

I am grateful to Dr. Andrew Rinzler and his group members for their support for Raman analysis. I would also like to thank Gerald Bourne for discussions concerning Nanoindentation. Additional thanks go to Hyungjin Bae and Dr. Yi-yeon Kim for measurement and discussions of AFM results. Thanks are due to Dr. Valentin Craciun, Seungwoo Lee, and Eric Lambers for helping with the XPS analysis and Kwanghoon Kim for collecting PL data. This assistance was fundamental for this work.

I am indebted to my friends and coworkers for their friendship and encouragement throughout my stay in Gainesville. Special thanks go to Chad Essary for giving me a lot of advice on my written English. I also thank Han Ho Choi, Su-Ho Jung, Jeremiah Abiade, and Karthik Ramani. I am also greatly appreciative of my senior group members, Dr. Kyu-Kong Cho, Dr. Jaeyoung Choi, Dr. Kyose Choi, Dr. Seungmahn Lee, Dr. Wonseop Choi, Dr. Hyucksoo Yang, Dr. Joodong Park, Dr. Won-Seok Kim, Dr. Mike Olinger, Dr. Frank Kelly, Dr. Josh Howard, and Dr. Nabil Bassim. Also, I want to thank Dr. Kyupil Lee, Dr. Jungsik Bang, Dr. Ki-Hong Lee, Dr. Heesun Yang, Dr. Jungmin Cho, Jinho Kim, Dr. Junyoung Park, and Jamie Rhodes for always having been my good friends. Of course, very special thanks go to Mrs. Margaret Rafton, who always took care

of all our group members with love, and she was a good friend of my Mother, too. I thank everyone very much. I will never forget my life in Gainesville.

TABLE OF CONTENTS

page

ACKNOWLEDGMENTS iv

LIST OF TABLES viii

LIST OF FIGURES ix

ABSTRACT xii

CHAPTER

1. INTRODUCTION 1

2. LITERATURE REVIEW 4

2.1. Carbon 4
2.1.1. Nucleus and Electron Configuration of Carbon Atoms 4
2.1.2. Carbon allotropes 7
2.1.2.1. Diamond 7
2.1.2.2. Graphite 8
2.1.2.3. Fullerenes 8
2.1.2.4. Amorphous Carbon 9
2.2. Diamond-Like Carbon (DLC) 9
2.3. Deposition Methods 10
2.3.1. Ion Beam Deposition 11
2.3.2. Mass Selected Ion Beam Deposition 11
2.3.3. Sputtering 12
2.3.4. Cathodic Arc 13
2.3.5. Plasma Enhanced Chemical Vapor Deposition 14
2.4. Pulsed Laser Deposition 15
2.4.1. Principle of Excimer Lasers 15
2.4.2. Basics of PLD 15
2.4.3. Advantages of PLD 15
2.4.4. Disadvantages of PLD 16
2.4.4.1. Particulates 17
2.4.4.2. Angular distribution 19
2.5. Growth Mechanism of Amorphous Carbon Films 20

3. GROWTH AND CHARACTERIZATION OF LOW STRESS DIAMOND-LIKE CARBON FILMS BY A MULTI-CYCLE PROCESS 34

3.1. PLD Grown Diamond-like Carbon Films 34
3.2. Experimental Procedures 36
3.2.1. Film Synthesis 36
3.2.2. Film Characterization 36
3.3. Results and Discussion 37

4. GROWTH AND CHARACTERIZATION OF AMORPHOUS CARBON NITRIDE FILMS WITH LOW NITROGEN CONCENTRATION 71

4.1. Amorphous Carbon Nitride Films 71
4.2. Experimental Procedures 72
4.2.1. Film Synthesis 72
4.2.2. Film Characterization 73
4.3. Results and Discussion 74

5. INFLUENCE OF DEPOSITION TEMPERATURE ON THE MICROSTRUCTURES AND PROPERTIES OF AMORPHOUS CARBON FILMS 99

5.1. Effect of Substrate Temperature 99
5.2. Experimental Procedure 99
5.2.1. Film Synthesis 99
5.2.2. Film Characterization 100
5.3. Results and Discussion 100

6. MECHANICAL PROPERTIES OF AMORPHOUS CARBON FILMS MEASURED BY NANOINDENTATION MEASUREMENTS 115

6.1. Microstructure Related Mechanical Properties 115
6.2. Nanoindentation Test 116
6.2.1. Indentation Hardness and Modulus 116
6.2.2. Load-Depth Compliance Curves 117
6.3. Results and Discussion 119

7. CONCLUSION 138

LIST OF REFERENCES 141

BIOGRAPHICAL SKETCH 148

LIST OF TABLES

Table page

2-1. The bond length and energy of various carbon couples 28

4-1. XPS results of (a) C 1s and (b) N 1s for CN_x at different laser fluences. 82

4-2. XPS results of (a) C 1s and (b) N 1s for CN_x at different nitrogen pressures 83

LIST OF FIGURES

Figure page

2-1. Different types of carbon bonding hybridizations 29

2-2. A ternary phase diagram of bonding in amorphous carbon alloys. 30

2-3. Schematic of various deposition systems 31

2-4. Schematic of different bonding characteristic on ion energy 32

2-5. Schematic of the basic processes in subplantation model 33

3-1. Schematic of the PLD chamber 49

3-2. Raman spectra of DLC at different laser fluences 50

3-3. A fitting of DLC Raman spectrum by D-peak and G-peak 51

3-4-1. Fitted Raman spectra of DLC at (a) 2.4 and (b) 4.0 J/cm^2. 52

3-4-2. Fitted Raman spectra of DLC at (c) 5.6 and (d) 7.2 J/cm^2. 53

3-5. Dependence of I_D/I_G and G-width on laser fluence. 54

3-6. Dependence of G-peak and D-peak positions on laser fluence. 55

3-7. Auger spectrum of DLC by PLD 56

3-8. IR stretching of DLC by PLD 57

3-9. XPS survey scan of DLC by PLD 58

3-10. A fitting of XPS C 1s peak of DLC. 59

3-11-1. XPS C 1s peak of DLC at (a) 2.4 and (b) 4.0 J/cm^2 60

3-11-2. XPS C 1s peak of DLC at (c) 5.6 and (d) 7.2 J/cm^2 61

3-12. Variation of sp^3 in DLC at different laser fluences 62

3-13-1. 2-D AFM images of DLC at (a) 2.4 and (b) 4.0 J/cm^2 63

3-13-2. 2-D AFM images of DLC at (c) 5.6 and (d) 7.2 J/cm^2 64

3-14-1. 3-D AFM images of DLC at (a) 2.4 and (b) 4.0 J/cm^2 65

3-14-2. 3-D AFM images of DLC at (c) 5.6 and (d) 7.2 J/cm^2 66

3-15. Dependence of (a) RMS and (b) sp^3 % on laser fluence 67

3-16. Buckling patterns on highly stressed DLC 68

3-17. Stress of the multi-cycle deposited DLC at different laser fluences 69

3-18. XPS C 1s peak of a highly stressed DLC by single cycle PLD 70

4-1. Dependence of N content on laser fluence 84

4-2. Dependence of N content on the NPP 85

4-3. C 1s peaks of *N1* CN_x at different laser fluences 86

4-5. C 1s peaks of CN_x at different NPP 88

4-6. N 1s peaks of CN_x at different NPP 89

4-7. Summary of XPS fitting from Table 4-2. 90

4-8. Raman spectra of CN_x at different laser fluences 91

4-9. Raman spectra of CN_x at different laser fluences 92

4-10. Summary of CN_x Raman results at different laser fluences 93

4-11. Raman spectra of CN_x at different NPP. 94

4-12. 3-D AFM images of CN_x at *N1*: (a) 2.4 and (b) 5.6 J/cm^2 95

4-13. Dependence of RMS of *N1* CN_x on laser fluence 96

4-14. AFM images of *N2* CN_x at 5.6 J/cm^2 97

4-15. Raman of particulate on *N2* CN_x at 5.6 J/cm^2. 98

5-1. Dependence of the N content in CN_x on deposition temperature 105

5-2. XPS C 1s spectra of DLC at different deposition temperatures. 106

5-3. XPS C 1s spectra of *N1* CN_x at different deposition temperatures. 107

5-4. Raman spectra for DLC at different deposition temperatures. 108

5-5. I_D/I_G and G-position vs. deposition temperature 109

5-6. 2D AFM images of DLC at (a) 200 and (b) 300°C. 110

5-7. 3D AFM images of DLC at (a) 200 and (b) 300°C. 111

5-8. 2D AFM images of *N1* CN_x at (a) 200 and (b) 300°C. 112

5-9. 3D AFM images of *N1* CN_x at (a) 200 and (b) 300°C. 113

5-10. AFM images of thermally degraded *N3* CN_x at 450°C. 114

6-1. Load-displacement curves for DLC films at different laser fluences.....124

6-2. Schematic of Triboindenter® with Triboscope® by Hysitron. 125

6-3. H and E_r of multi-cycle deposited DLC on Si substrates. 126

6-4. Displacement and time sequence for the nanoindentation. 127

6-5. H and E_r of bare Si and DLC 128

6-6. *In-situ* images of nanoindentation process on DLC 129

6-7. H and E_r of DLC at different laser fluences. 130

6-8. Change in mechanical properties of DLC by different laser fluences.....131

6-9. H and E_r of CN_x at different laser fluences 132

6-10. H and E_r of DLC and *N1* CN_x at different laser fluences.....133

6-11. H and E_r of DLC at different temperatures. 134

6-12. Temperature dependence of H and E_r of DLC 135

6-13. Load-displacement curve of *N3* CN_x at 450°C.....136

6-14. H and E_r of *N3* CN_x at 450°C. 137

Abstract of Dissertation Presented to the Graduate School
of the University of Florida in Partial Fulfillment of the
Requirements for the Degree of Doctor of Philosophy

GROWTH AND CHARACTERIZATION OF LOW STRESS AMORPHOUS CARBON FILMS BY PULSED LASER DEPOSITION PROCESS

By

Sang Hyun Yoon

December 2004

Chair: Rajiv K. Singh
Major Department: Materials Science and Engineering

Low stress amorphous carbon films have been studied for various protective coating applications. A graphite target of 99.99% purity was ablated by a KrF excimer laser of 248 nm wavelength to provide the carbon source. For the deposition of diamond-like carbon films, a multi-cycle process (10 cycle repetition of 30 sec deposition followed by 30 sec relaxation period) was used to relieve the high internal stress, which is known to develop during the coating condensation. High purity (99.999%) nitrogen gas was used to produce amorphous carbon nitride films. The microstructure changes of the amorphous carbon films were closely observed with Raman spectroscopy, X-ray photoelectron spectroscopy, and atomic force microscopy. It has been revealed that films deposited at higher laser densities exhibited more sp^3 bonding contents with lower root mean square roughness values. However, no sign of coating failure due to high stress was observed from the multi-cycle deposited diamond-like carbon films and the single-cycle deposited amorphous carbon nitride films. Residual stress values of these films were measured at

only ~3 GPa. Nanoindentation measurements confirmed that the microstructures and the mechanical properties of these amorphous carbon films were effectively controlled by various process parameters for specific coating applications. Thermal degradation has been observed from amorphous carbon nitride film deposited at 450°C.

CHAPTER 1
INTRODUCTION

Amorphous carbon films represent noteworthy thin films whose properties can be varied over a wide range of structures and compositions. Diamond-like carbon (DLC) and amorphous carbon nitride (CN_x) films are the most studied structures among them. Both DLC and CN_x are metastable materials and have to be prepared under ion bombardment of the growing films. Studies of DLC have been performed extensively since Aisenberg and Chabot first prepared DLC [Ais71], and there has been a great development in understanding the growth mechanisms, material properties and usage of DLC in industrial applications [Gri99, McK93]. At the same time, other forms of amorphous carbon films, such as CN_x, DLN (diamond-like nanocomposite), etc. have been also the subject of intensive studies due to their intrinsic film properties, such as high hardness, chemical inertness, electrical and optical properties [Gor94, Pan95, Pap94]. The most attractive advantage of amorphous carbon films is the possible controllability of properties over a wide range [Gri99, Rob02]. Depending on the deposition techniques and process conditions, a variety of amorphous carbon films intermediated between graphite and diamond can be produced [Mck93, Par02]. This can be realized because both sp^2 and sp^3 configurations exist in amorphous carbon films. Controlling the combination of these bonding types during the deposition process can produce the amorphous carbon films of various properties [Erd01, Rob02, Wei99].

Diamond-like carbon (DLC) exists in the form of either amorphous carbon (a-C) or of hydrogenated amorphous carbon (a-C:H). With their unique properties such as high

hardness, low friction, chemical inertness and optical transparency, DLC films are used in many industrial applications. Pulsed laser deposition (PLD) has been used as one of the promising methods to deposit unhydrogenated DLC films. Pulsed laser deposited DLC contains relatively high contents of sp^3 hybridized carbon atoms [Tab99, Yam98]. However, the high intrinsic stress in DLC with high sp^3 content has been a major drawback to be solved to increase its validity in many applications.

Amorphous carbon nitride (CN_x) films also have been studied extensively since Liu and Cohen predicted that a carbon nitride, β-C_3N_4 phase should exhibit superior mechanical properties [Liu89, Liu90]. However, amorphous CN_x films with low N concentration are attracting more interest in these days [Muh99, Rie00, Sil97, Tet96]. This is attributed to the many attractive properties of CN_x, such as low internal stress [Sjo96], relatively high hardness [Tan98], etc. Among different types of deposition methods, PLD is a popular method to deposit CN_x films due to the high ion energy and the possibility of deposition of carbon nitride films with higher crystallinity [Che02a]. Although there have been numerous publications on the synthesis and properties of CN_x films [Che02a, Che99, Wie01, Zha01], the amorphous nature of the film, together with the complex bonding structures due to nitrogen inclusion, makes it hard to reach a clear understanding of CN_x films.

In Chapter 2, the general background on amorphous carbon films will be introduced, highlighting the various types of carbon based materials, their growth mechanism, and deposition methods. The growth and characterization of the two most representative amorphous carbon films, namely DLC and CN_x, will be presented in Chapter 3 and 4, respectively. In Chapter 3, a multi-cycle process of PLD will be

introduced to produce high quality (sp^3-rich) DLC films free of delamination induced coating failure. Formation of low density (sp^2-rich) thin surface layer at the end of each cycle is expected to help release the high intrinsic stress compiled during the subplantation growth mode. Also, a systematic study of CN_x films by various techniques, such as XPS and Raman spectroscopy, will be performed to clarify the local bonding structure and the properties of CN_x films in Chapter 4. The effect of deposition temperature on the structure and properties of amorphous carbon films will be precisely observed with AFM and other techniques to check the thermal stability of these materials (Chapter 5). Finally, the last chapter (Ch. 7) will be devoted to evaluate the mechanical properties of amorphous carbon films by nanoindentation test. Hardness (H) and elastic modulus (E) will be measured and used to confirm the structure change of amorphous carbon films observed in earlier chapters. This will provide the fundamental information for deciding the feasibility of coating applications.

CHAPTER 2
LITERATURE REVIEW

2.1. Carbon

2.1.1. Nucleus and Electron Configuration of Carbon Atoms

Carbon can exist as allotropes of different forms with versatile properties, such as diamond (the strongest crystal and hardest material), graphite (one of the best solid lubricants), activated charcoal (one of the best gas absorbers), vitreous carbon (very efficient helium gas barrier), and carbon fibers (the highest strength fiber), etc. [Fie79, Pie93]. The different properties of these carbon-based materials result from their different structures consisting of various carbon bonding combinations. This is possible because carbon is able to exist in three different hybridizations, sp^3, sp^2, and sp^1 (Fig. 2-1) [Erd01, Pie93, Rob86].

Diamond has the highest atomic density of any solid at ambient pressure due to sp^3 configuration (each of the four valence electrons of a carbon atom is assigned to a tetrahedrally directed sp^3 orbital) (Fig. 2-1(a)). This configuration gives the strong σ bond to an adjacent atom. The strong directional sp^3 bonding of diamond provides many unique properties such as the highest elastic modulus, hardness, and thermal conductivity [McK91, Rob92]. A wide optical band gap and a very low thermal expansion coefficient are also contributed to the sp^3 configurations of diamond [Erd01, Rob02].

Graphite has a lower atomic density than diamond and exhibits the three-fold coordinated sp^2 configuration (Fig. 2-1(b)). In sp^2 configuration, three of the four valence electrons enter trigonally directed sp^2 orbitals. These electrons form σ bonds in the same

plane. The fourth electron of sp^2 atom lies in a $p\pi$ orbital forming a weaker π bond with a π orbital on neighboring atom. The π bonds are delocalized and graphite becomes an electrical conductor in the plane. The weak interlayer bonding of graphite allows it to be used as a solid lubricant [Pie93, Rob02].

In the sp^1 configuration, two of the four valence electrons enter σ orbitals, each forming a σ bond directed along the $\pm x$-axis, and the other two electrons enter $p\pi$ orbitals in the y and z directions, as shown in Fig. 2-1 (c).

When looking into the electronic structure of elemental carbon more closely, carbon consists of six protons and neutrons in the nucleus, as well as corresponding six electrons. The ground state of carbon's electronic configuration can be stated as $1s^2 2s^2 2p^2$, 2 electrons in the K shell (1s) and 4 in the L shell (2s and 2p). In order to possess the electron configuration of tetrahedral symmetry (i.e., diamond), the carbon atom must be transformed to a form composed of four valence electrons, not two. This can happen by forming hybrid atomic orbitals, in which the electronic arrangement of L shell in ground state is modified as one of the 2s electron is promoted to the higher orbital 2p. Now, one 2s and three 2p orbitals will form four hybrid sp^3 orbitals, resulting in four valence states instead of two. The four hybrid sp^3 orbitals have identical shape with different spatial orientation as shown in Figure 2-1(a). Connecting the end points of these vectors (orientation of maximum probability) forms a regular tetrahedron with equal angles (109.5°) to each other. The four sp^3 valence electrons, together with the small size of the atom, result in strong covalent bonds, since four of the six electrons of the carbon atom form bonds. The heavily lopsided configuration of the sp^3 orbital allows a substantial overlap and a strong bond when the atom combines with a sp^3 orbital from another

carbon atom since the concentration of bonding electrons between the nuclei minimizes the nuclear repulsion and maximizes the attractive forces between themselves and both nuclei. By convention, a directional orbital such as the sp^3 is called a sigma (σ) orbital, and forms a sigma bond. Each tetrahedron of the hybridized carbon atom combines with four other hybridized atoms to form a three dimensional, entirely covalent, lattice structure. From the geometrical standpoint, the carbon nucleus can be considered as the center of a cube with each of the four orbitals pointing to four alternation corners of the cube [Gri99, Rob93]. These sp^3 orbitals are the key to constitute diamond and aliphatic compounds [Pie93].

On the other hand, the sp^2 (or trigonal) orbital is the basis of all graphite structures and aromatic compounds [Pie93]. The mechanism of the sp^2 hybridization is somewhat different from that of the sp^3 hybridization [Rob02]. The arrangement of electrons in the ground state L shell is modified as one of the 2s electrons is promoted and combined with two of 2p orbitals to form three sp^2 orbitals and one un-hybridized free (or delocalized) p orbital electron. The three identical sp^2 orbitals are in the same plane, and their orientation of maximum probability forms a 120° angle from each other (Fig. 2-1 (b)). The fourth orbital, i.e., the delocalized non-hybridized p electron, is directed perpendicularly to the plane of the three sp^2 orbitals and becomes available to form the subsidiary π bond with other atoms. The sp^2 bond is also a covalent bond, which is very strong due to the three sp^2 valence electrons and the small size of the atom. The lopsided configuration of the sp^2 orbital allows a substantial overlap with other sp^2 orbitals. Like the sp^3 orbital, the sp^2 is directional and is called a σ orbital, forming a strong σ bond. Each sp^2 hybridized carbon atom combines with three other sp^2-hybridized atoms to form

a series of hexagonal structures, all located in parallel planes [Rob02]. The fourth valence, that is, the free delocalized electron, is oriented perpendicular to this plane. Unlike the σ orbital, it is non-symmetrical and is called by convention a phi (π) orbital. It is available to form a subsidiary π bond. In a sp^2 structure such as graphite, the delocalized electron can move readily from one side of the plane layer to the other, but cannot easily move from one layer to another. As a result, graphite is anisotropic. Table 2-1 shows the bonding energy and length of various carbon couples [Pie93].

2.1.2. Carbon allotropes

The carbon allotropes are generally classified into three major categories. As mentioned briefly in the previous section, there are the sp^3 structured materials, such as diamond and lonsdaleite, and the sp^2 structured materials such as graphite. The fullerenes are another major type of carbon allotropes. The mixed structures including both sp^3 and sp^2 bondings can be produced by low pressure and low temperature process [Fie79]. These materials exhibit amorphous structure including diamond-like carbon materials [Gri92, McK91].

2.1.2.1. Diamond

All of the four bonding electrons form strong σ bonds in tetrahedral sp^3 bonding structure. Each carbon atom forms σ bonds tetrahedrally with four other carbon atoms in the diamond space lattice. The bonding length and angle are 0.154 nm and 109.5°, respectively. Coupled with the fact that diamond is a macromolecule of entirely covalent bonded carbons, the high strength of sp^3 bondings give the diamond its unique physical properties: high atomic density, extreme hardness, transparency, and extremely high electrical resistivity (10^{16} Ω-cm), etc. [Fie79, Rob02].

2.1.2.2. Graphite

The outer 2s, $2p_x$, and $2p_y$ orbitals hybridize in a manner to give three co-planar sp^2 orbitals forming three σ bonds and a p-type π orbital ($2p_x$) perpendicular to the sp^2 orbital plane. Graphite consists of hexagonal layers separated from each other by a distance of 0.34 nm. Each carbon atom forms σ bonds with the other three carbon atoms; they are separated by a distance of 0.142 nm within a hexagonal plane [Fie79, Rob02]. These planes are held together by weak van der Waals bonding which explains why graphite is soft along the sp^2 plane. The localization of π orbital gives rise to π-π^* density of states which constitute overlapping valence and conduction bands. This accounts for the electric conductivity of graphite and its slight metallic luster [Gri99]. It is interesting to note that the (111) planes in diamond resemble graphite planes but differ in that they are puckered and have no π bonding [McK93].

2.1.2.3. Fullerenes

The C_{60} and C_{70} are the most accessible members of the closed-cage molecule family called fullerenes [Kro85]. This carbon allotrope consists entirely of the sp^2 hybridized carbons. Each fullerene C_n consists of 12 pentagonal rings and m hexagonal rings such that $m = (n-20)/2$. The σ bonds are warped such that fullerene has a highly strained structure and the molecule is rigid. One noteworthy feature of this molecule is that there is a tendency to avoid double bond formation within strained pentagonal rings adjacent to benzoid rings. Thus electron delocalization is poor and hence, contrary to graphite, C_{60} solid has a band-gap. It also has been shown that C_{60} transforms to bulk polycrystalline diamond at room temperature when subjected to non-hydrostatic compression of 20 ± 5 GPa [Rob02]. It is interesting to note that fullerenes are formed in

a cathodic arc process involving carbon electrodes under high pressure of argon gas up to several atmospheres.

2.1.2.4. Amorphous Carbon

Amorphous carbon is the generic term used to describe the most disordered carbon films in the metastable state without any long range order [Gri99, McK93, Rob92]. Although there is no long range order present, short and medium range orders exist and endow crystalline diamond-like physical properties to amorphous carbon [Rob02]. Therefore, these structures are generally called diamond-like carbon (DLC). It has been proved that the short/medium range order of amorphous carbon is very close to that of its crystalline counterpart by examining the nearest and next nearest neighbor distances [McK91]. Material properties of amorphous carbon change when using different deposition techniques or even varying the deposition conditions within a single technique. Therefore, variety forms of non-crystalline carbon forms can be produced with well-controlled process parameters. A detailed description on amorphous carbon will be presented in the following section.

2.2. Diamond-Like Carbon (DLC)

Since Aisenberg and Chabot reported the term *diamond-like carbon* (DLC) for ion beam deposited carbon films which exhibited some physical properties similar to diamond [Ais71], large efforts have been made on the deposition and characterization of DLC and their variants [Rob91]. At the same time, not a little research has been concentrated on finding a useful application of these DLC films [Sil02]. Deposition of thin carbon films was focused on the growth of polycrystalline diamond films in the early days [Rob91]. However, the high surface roughness limits the utilization of polycrystalline diamond films for some applications, such as protective coatings on

optical window. This is mainly due to the excessive light scattering at the rough surface. Also, the high substrate temperature (> 700°C) delimitates the selection of substrates. Such technical problems have led to the development of alternative materials [Rob94].

Amorphous carbon films, generally called diamond-like carbon, have emerged as a strong candidate for the alternative to diamond in a number of applications. DLC exhibits optical smoothness due to its amorphous structure and can be deposited at temperatures lower than 200°C. DLC offers a good combination of attractive properties such as controllable optical band gaps, high electrical resistivity, high breakdown strengths, a high hardness and high wear resistance. This can be realized by choosing the optimal deposition method and process parameters. Various deposition techniques will be reviewed in the following section. Due to the variety of combinations of bond hybridizations in amorphous carbon films, the different terminologies are used to indicate DLC films. DLC structures can be divided into two large categories depending on the carbon sources used to produce them: hydrogenated and non-hydrogenated films. Jacob and Moller used a ternary phase diagram to display the compositions of the various types of DLC films, shown in Fig. 2-2 [Jac93].

2.3. Deposition Methods

Various deposition methods have been used to prepare amorphous carbon films: ion beam deposition, sputtering, pulsed laser ablation, plasma enhanced CVD, etc. Various deposition systems are schematically shown in Fig. 2-3. All methods for the deposition of amorphous carbon films are non-equilibrium processes, commonly featured by interaction of energetic species with the surface of growing carbon film, which induces the sp^3 bonding [Rob92, Erd01]. It is well known that the properties of

amorphous carbon films deposited under ion bombardment conditions tend to pass through three regimes as a function of ion energy as shown in Fig. 2-4 [Rob91]. Depending on the deposition technique used, amorphous carbon films with different carbon hybridization ratio and hydrogen concentrations can be achieved, resulting in a wide range of film properties. Therefore, the fundamental understanding and the proper selection of deposition methods can be regarded as very important tasks to be done for the successful production of DLC films of required properties.

2.3.1. Ion Beam Deposition

The ion beam deposition system was used to prepare the first DLC films [Ais71]. In a typical ion beam deposition system, carbon ions are produced by the plasma sputtering of a graphite cathode in an ion source. Alternatively, as in the Kaufman source, a hydrocarbon gas such as methane is ionized in plasma [Rob02]. An ion beam is then extracted through a grid from the plasma source by a bias voltage. The carbon ions or hydrocarbon ions are then accelerated to form the ion beam in the high vacuum chamber. In both cases, the ion source runs at a finite pressure, so that the beam also contains a large flux of unionized neutral species. This can reduce the flux ratio of ions to neutrals to as low as 2 – 10 %. Ion beam sources tend to run best at higher ion energies of 100 – 1000 eV.

2.3.2. Mass Selected Ion Beam Deposition

It is desirable to have a controlled deposition from a single ion species with well-defined ion energy. This is achieved by mass selected ion beam deposition (MSIB) [Lif95]. In mass selected ion beam deposition, a mono-energetic beam of carbon ions is produced by using a mass analyzer between the ion source and the substrate. Carbon ions are produced in an ion source from a graphite target, such that the spread of ion energies

is small, 1 – 10 V. The ions are then accelerated to 5 – 40 kV and passed through a magnetic filter. This filters out any neutrals and selects ions with a specific *e/m* ratio of the C^+ ion. The ion beam will diverge because of its Coulombic repulsion. The ions are then decelerated to the desired ion energy by electrostatic lens, and the beam is focused onto the substrate in a vacuum of order 10^{-8} Torr to produce amorphous carbon film with high fraction of sp^3 bondings (ta-C). The advantages of MSIB are that it gives the controllable deposition species and energy, the filtering out of non-energetic species, and the ability to dope by switching the ion species. However, as a practical process for producing quantities of material, very low deposition rate (~0.0001 nm/s) and high cost renders MSIB unattractive [Lif95, Rob02].

2.3.3. Sputtering

Sputtering is a widely used industrial process for the DLC deposition [Cho90, Sch96]. The most common form uses the dc or rf sputtering of a graphite electrode by an Ar plasma. Because of the low sputter yield of graphite, magnetron sputtering is often used to increase the deposition rate [Erd01, Rob02]. Magnets are placed behind the target to cause the electrons to spiral and increase their path length, and thus to increase the degree of ionization of plasma. As ion bombardment helps the formation of sp^3 bonding, the magnetic field can be configured to pass across to the substrate, so this causes the Ar ions to also bombard the substrate, to give an 'unbalanced magnetron'. A dc bias can be applied to the substrate to vary the ion energy. The a-C:H can be produced by reactive sputtering, by using a plasma of Ar and hydrogen or methane, and a-CN_x can be produced using an argon-nitrogen plasma [Rob02]. Alternatively, a beam of Ar ions can be used to sputter from the graphite target to create the carbon flux in ion beam sputtering [Cuo91]. A second Ar ion beam can be used to bombard the growing film, to densify the

film or encourage sp^3 bonding. This is called ion beam assisted deposition (IBAD) or ion plating [Rob02].

A disadvantage of sputtering is, like ion beam deposition, that it can have a relatively low ratio of energetic ions to neutral species, so that it does not produce the hardest DLC films. However, sputtering methods with a very high fraction of ions have been developed to produce a-C with a relatively large sp^3 fraction [Cuo91, Sch96].

2.3.4. Cathodic Arc

An arc is initiated in a high vacuum by touching the graphite cathode with a small carbon striker electrode and withdrawing the striker. This produces energetic plasma with a high ion density of up to 10^{13} cm^3. The cathode spot is small, 1 – 10 μm and it carries a very high current density of 10^6 – 10^8 A-cm^{-2}. The spot is formed by an explosive emission process. This creates particulates as well as the desired plasma. The particulates can be filtered by passing the plasma along a toroidal magnetic filter duct. This is known as filtered cathodic vacuum arc (FCVA) [Bro98]. The toroidal currents produce a magnetic field of about 0.1 T along the axis of the filter. The electrons of plasma spiral around the magnetic field lines and so they follow them along the filter axis. This motion produces an electrostatic field, which causes the positive ions to follow the electrons around the filter, resulting in an amipolar transport of the plasma around the filter [Rob02]. The particulates cannot follow the field and they hit the walls and baffles on the walls. Alternatively, in the open filter system, the particulates pass between the coils out of the filter zone into the chamber [Bro98]. The neutrals also hit the walls, so the filter raises the plasma ionization from about 30% to nearly 100% at the filter exit. A dc or rf self-bias voltage applied to the substrate is used to increase the incident ion energy. The

FCVA should be operated at a background pressure of ~ 10^{-8} Torr, but this may rise to 10^{-5} when the plasma is running [Par02, Rob02].

The FCVA produces highly ionized plasma with an energetic species of a fairly narrow ion energy distribution. However, filtering is not sufficient for some applications. Unstable spot is another disadvantage of FCVA. The particulates are generally submicron-size particles. These can still pass through the filter section by bouncing off the walls [And97].

2.3.5. Plasma Enhanced Chemical Vapor Deposition

The other popular deposition method for deposition of amorphous carbon films is radio frequency (rf) PECVD [Koi90, Wei98]. Plasma is produced between two electrodes of different sizes by applying *RF* power. The higher mobility of electrons than that of ions in plasma develops a sheath next to the electrodes with an excess of ions, resulting in positive space charge. Therefore, a positive voltage is generated with respect to the electrodes [Rob02]. The smaller electrode with smaller capacitance acquires the larger bias voltage and becomes negative with respect to the larger electrode. This smaller electrode will make the substrate electrode. The positive ions are accelerated by the negative sheath voltage to give the bombardment needed to create the sp^3 bonding. In order to deposit amorphous carbon films with diamond-like characteristics, the process pressure should be kept at the lowest possible level to maximize the ion to radical fraction of the plasma [Rob02]. There is a wide distribution of ion energies due to the collisions when being accelerated across the sheath. It is desirable to use a low pressure to minimize these collisions to maintain a narrow ion energy distribution. However, it is not possible for conventional PECVD to use lower pressure, as the plasma can not be sustained [Rob02].

2.4. Pulsed Laser Deposition

2.4.1. Principle of Excimer Lasers

Excimer is an acronym for EXCIted diMER, a rare gas dimmer based on the rare gas halogen. Excimer laser is high pressure, pulsed gas laser that gives rise to UV light with a wide range of wavelengths from 193 to 351 nm. Energy is pumped by avalanche electric discharge excitation in a gas mixture consist of (i) a rare gas (Ar, Kr, Xe), (ii) a halogen gas (F, Cl), and (iii) a buffer gas (He, Ne). The pumping generates ionic species and electrically excited species that react chemically and produce Excimer molecules. Once Excimer molecules are formed, they will decay rapidly with emitting photons via the transition from upper electronic state to lower ground state. These emitted photons are the Excimer lasers with wavelengths in the UV range.

2.4.2. Basics of PLD

The PLD vacuum chamber includes a target holder and a substrate holder [Che94]. Energetic laser beams focused by a set of optical components are directed to the target through the UV-transmission window. When the laser beam impinges on the target, photons are absorbed by the surface of the target, resulting in the evaporation of target materials. Evaporants produce a plume consisting of a mixture of atoms, molecules, and electrons. The plume expands rapidly from the target surface forming a nozzle jet with a highly directional flow normal to the target surface. The substrate is mounted in the path of the plume. Each laser pulse forms a new plume from the target and deposits new material on the film surface.

2.4.3. Advantages of PLD

Recently, a summary of advantages and disadvantages of PLD process has been reported [Low98]. If appropriate laser energy density, beam spot size, and shape are

selected, stoichiometric transfer of material from target to growing film can occur within a finite deposition angles. The stoichiometric transfer can be achieved only if the laser energy density is high enough to form laser generated plasma. This laser generated plasma induces the erosion of a target material resulting in the stoichiometric transfer of all constituents of a complex material.

Since there is no electron beam or hot filament in the deposition chamber, it is possible to deposit film through reactive deposition in ambient gas. Simple compound film can be obtained by reactive deposition if proper ambient gas is introduced into the chamber. Also, collisions with ambient gas molecules can be used to control the ablation beam kinetic energy that affects the point defect concentration in the film [Che94].

PLD Film growth is achieved within laser-generated plasma. A variety of species in the plume possess kinetic and potential energies that can increase sticking coefficients, surface mobilities of adatoms, and nucleation due to high energy chemical reactions. Thus, epitaxial growth of films can be obtained under the proper experimental conditions such as appropriate substrate temperature. Also, growth of multilayered epitaxial heterostructures or superlattices is possible by using chemically complex multi-targets with rapid target exchangers [Che94, Low98].

2.4.4. Disadvantages of PLD

There have been two main drawbacks limiting the development of PLD technique: the formation of *particulates* and the production of an *angular distribution* of ablated species. Particulates can be a serious problem for semiconductor films and optical films, since they can produce defects and scattering centers those decrease carrier mobility, shorten the mobility life time, and decade the damage threshold of optical films.

Production of an angular distribution of ablated material makes it hard to obtain films with uniform thickness [Che94].

2.4.4.1. Particulates

Three mechanisms have been reported for particulate formation, depending on its phase (solid, liquid, vapor) when ejected from the target material [Che94]. Micro-cracks in a fresh target or crater edges by laser irradiation are mechanically weak and have a tendency to dislodge from the target due to the laser-generated thermal and mechanical shocks. The sizes of particulates produced by these extrications are in micron/submicron range. The shapes of particulates tend to be spherical if they are created by melting during laser irradiation, otherwise irregular shapes are obtained.

There are two possible mechanisms to explain the particulate formation from the liquid phase: the splashing of molten layer generated by superheating of surface layer, and the laser induced recoil pressure generated by rapid surface evaporation from the molten liquid layer. The particulates forming from the liquid phase exhibit spherical shape with size of a few microns.

The condensation from the vapor phase produces very fine particulates, in the range of nanometers. When the pressure of ambient gas is sufficiently high, a large number of collisions with the gas modules result in nucleation and growth of fine particulates before they arrive at the substrate. The shape of the particulates forming from the vapor phase is either spherical or polygonal.

It has been reported that particulate generation is mainly affected by both the laser parameters and the material properties [Che94]. The density and size of particulates increase with the laser energy density above the threshold laser energy density for

particulate generation. A simple way to decrease the number of particulates is to reduce the laser power density below the threshold value for the splashing of the molten layer.

Not only the laser energy density but also the laser wavelength can affect the density and size of particulates. Generally, the density and size of particulates produced by longer laser wavelength are much higher than those produced by shorter laser wavelength. Because photons with short wavelength penetrate less into the target due to absorption, the ejection of molten material occurs only within a very thin layer. Therefore, the most effective way to minimize the density and size of particulates is to use short wavelength such as KrF (248 nm) or ArF (193 nm) excimer lasers.

The size of very fine particulates produced by condensation from the vapor species is affected by the ambient gas pressure. The size of particulates increases with increasing ambient pressure because of the increased frequency of collisions between the vapor species and ambient gas molecules leads to the nucleation and growth of fine particulates before they reach the substrate. Since the growth of fine particulates occurs by diffusion, the longer the residence time in vapor the larger the particulate. Thus, the particulate formed at a long distance between substrate and target is larger than those forming from at a short distance.

The properties of the target can also affect characteristics of particulates. A low-density target produces large irregular shaped particulates resulting from the fragments due to the weak bonding. On the other hand, a high-density target generates spherical shaped particulates by splashing [Che94]. As mentioned previously, a rough target surface gives rise to large particulate sizes. Therefore, selection of a high-density target

with smooth surface and target re-surfacing after laser irradiation are required to minimize the presence of particulates.

2.4.4.2. Angular distribution

The other disadvantage of PLD is the production of an angular distribution of ablated materials. Saenger reviewed the methods of measurement, experimental observation, and modeling related to angular distribution [Sae94]. The source angular distribution $f(\theta)$ and the film thickness distribution $D(\theta)$ are thought to exchange each other in PLD consideration. θ is the angle between the radial vector and target normal. For the case of deposited film on a flat substrate parallel to the target, the source distribution $f(\theta) = (\cos\theta)^P$ would generate a film thickness distribution $D(\theta) = (\cos\theta)^{P+3}$ [Che94]. Two methods have been used to measure the angular distribution from PLD: *film* based method and *probe* based method. In the film based method, the angular distribution $D(\theta)$ is simply measured by measuring the thickness of the film at each distance x from the ablation center axis and $\theta = \tan^{-1}(x/h)$. However, this method is based on the assumptions that the ablated particles have a unity-sticking coefficient and the depositing film is not re-sputtered by the incident flux of particles. The probe based method measures the source angular distribution with an ion probe or mass sensitive detector in which probe or detector measures the flux emitted from the target into different angles.

The angular distribution can be affected by various experimental parameters such as laser parameters, system geometry, target properties, and ambient gas [Sae94]. For the effect of focused spot size on the angular distribution, there is a clear nonequivalence between a single spot and a small spot scanned over the same area, the latter providing a

much broader than the former. This effect stems from the fact that forward peaking increases with the number of intra-plume collisions per particle.

The angular distribution is expected to remain constant with target-substrate distance when no collisions among particles occur in vacuum. However, a change in the source distribution with target-substrate distance has been observed for carbon [Gor89] in which a broader angular distribution was obtained at shorter distances. This phenomenon is attributed to the scattering of the incident flux by particles re-sputtered and reflected from the substrate. When an ambient gas is introduced, the plume angular distribution becomes broader since particles in the plume undergo collisions with the background gas resulting in the scattering of particles away from their original trajectories [Sae94].

More detailed measurements incorporate the variation in composition of film by PLD with angle from the center axis even though PLD has been known as a method that produces the same film composition (stoichiometry) [Che94]. If two assumptions (unity sticking coefficient and no re-sputtering) for the film based method are valid, the variation in film composition means that different chemical species in the plume have different angular distributions. The different angular distributions of different species in the plume are caused by discrepancy of the charge of species and their mass. Also, the sputtering by background gas can be one of the reasons that cause the variation in composition of film with angle [Che94, Sae94].

2.5. Growth Mechanism of Amorphous Carbon Films

High quality amorphous carbon films can be produced by specific deposition methods, such as PLD, MSIB, and FVA processes. All these techniques are using the flux of high energy ionic species. Amorphous carbons deposited with these equipments are known to possess high fraction of sp^3 hybridizations in their structure [Fal93]. The results

of neutron scattering support this finding, yielding the average C-C bond length of 0.153 nm and a bond angle of about 100°. This implies that the structure is a network dominated by tetrahedral bonding [Gas91]. Therefore, the material is referred to as amorphous diamond (a-D) or tetrahedral amorphous carbon (ta-C) in order to distinguish it from other forms of carbon structures, particularly evaporated a-C, in which its structure is almost composed of sp^2 bondings [McK91]. Hydrogen-free ta-C films, which contain more than 80% sp^3 bonding, has drawn considerable interest in recent years due to the unique properties such as extreme hardness, low friction coefficient, high wear resistance, transparency in the infrared range, high electrical insulation, chemical inertness, and excellent biocompatibility [Gri99, McK93]. In microscopic scale, ta-C films consist of sp^3 matrix embedded with nano-sized sp^2 clusters. Although the property of ta-C is largely dominated by tetrahedral sp^3 bonding, the sp^2 component is an important factor in the correlation of atomic structure with optical and electronic properties [Rob02].

There have been many models developed to examine the growth mechanism of amorphous carbon materials. However, there are still ongoing debates on the most energetically favorable configuration for the growth of films with high sp^3 fraction. The atomistic description of the growth mechanism has been developed as follows. Spencer et al. proposed various mechanisms such that the sp^3 sites arise from the sp^3/sp^2 mixture by a preferential sputtering of the sp^2 sites [Spe76]. However, Lifshitz et al. noted that this process would not work because of the sputtering yield of carbon [Lif90]. The sputtering yield depends primarily on an atom's cohesive energy, which is almost the same for the sp^2 and sp^3 sites. Therefore, there is only little difference in the sputtering yields between

sp^2 and sp^3 bonded carbons. Weissmantel suggested that the sp^3 bonding arose from a shock wave of the displacement spike of the ion cascade [Wei82]. This picture has some similarities to later models, but the shock wave is more appropriate to higher ion energies and higher ion masses. Lifshitz et al. used Auger analysis of the depth profiles of medium energy C ions incident on Ni substrates to show that the growth occurred at sub-surface [Lif90]. They denoted this process as *subplantation* (low energy surface implantation). They proposed that the sp^3 sites accumulate by a preferential displacement of sp^2 sites. Moller modeled this idea in more detail [Mol91]. The sp^2 and sp^3 atoms would be displaced at certain rates into interstitial sites, and then fall back at similar rates into sp^2 and sp^3 sites. The fraction of sp^3 sites increases if there is a preferential displacement of sp^2 atoms. This idea arose from some early estimates of the displacement threshold in graphite and diamond of 25 and 80 eV, respectively [Rob02]. However, more recent direct measurements of the displacement threshold find similar values for graphite (35 eV) and diamond (37 eV – 47 eV) [Koi92]. Therefore, this preferential displacement theory is not correct. It should be noted that the displacement threshold of graphite is quite anisotropic because of its layer structure, and Banhart still takes the displacement threshold for sp^2 sites to be lower [Ban99].

McKenzie et al. noted that sp^2 bonded graphite occupies 50% more volume than sp^3 bonded diamond [McK93]. This allows diamond stable at high pressures above Berman-Simon line in phase diagram of diamond and graphite. McKenzie and Davis proposed that the role of the ion beam is to create a compressive stress in the film, which will move the film above the B-S line and so stabilize the high pressure diamond (-like)

phase [Dav93, McK93]. Of course, in all these models, the phase once created is quenched into the growing film.

Robertson proposed that the subplantation created a metastable increase in density, which tends to cause the local bonding to change to sp^3 configuration [Rob94]. In this model, preferential displacement is not needed but only surface growth in a restricted volume is needed to get sp^3 bonding. The basic idea of subplantation has been proved with various numerical and analytical simulations [Kau92, Rob94]. The unsolved problem is the details of the relaxation process, which suppresses sp^3 bonding at higher ion energies and higher deposition temperatures.

In the energy range of interest, 10 – 1000 eV, the carbon ions have a range of a few nm and they loose their energy largely by elastic collision with the target atoms (nuclear stopping) [Rob94, Rob02]. The elastic collision of ions in solids can be simplified to the binary collision approximation, in which the collisions occur as a sequence of independent pair collisions. The cross section of collisions decreases as the energy is raised, as this is the repulsive part of the inter-atomic potential. Thus, an ion of zero-energy incident on a surface sees an impenetrable wall of touching spheres. At higher ion energy, the atomic radii decrease, so the interstices look wider. At some energy, the ion can pass through an interstice and so penetrate the surface layer. This ion energy is called the penetration threshold, E_P.

Another important ion energy is the displacement threshold, E_d. This is the minimum energy of an incident ion needed to displace an atom from a bonded site and create a permanent vacancy-interstitial pair. The surface of solid acts like an attractive

potential barrier of height E_B, the surface binding energy. This raises the kinetic energy of an ion by E_B when it enters the surface. Thus the net penetration threshold for free ion is

$$E_P \sim E_d - E_B \tag{2.1}$$

Now consider carbon ions incident on an amorphous carbon surface [Mol91]. A low energy ion will not have enough energy to penetrate the surface, so it will just stick to the surface, and remain in its lowest energy state which is sp^2. If the ion energy is higher than E_P, it has a probability to penetrate the surface, and enter a subsurface interstitial site. This will increase the local density. The local bonding will then reform around that atom according to this new density. The solid is amorphous, so the incident atom and the target atoms are equivalent [Rob02]. It is assume that in the highly energetic conditions of ion bombardment existing during film growth, atomic hybridizations will adjust easily to changes in the local density, and become more sp^2 if the density is low and more sp^3 if the density is high.

As the ion energy increases further, the ion range increases, and the ion penetrates deeper into the solid. A rather small fraction of this energy is used to penetrate the surface, and another fraction of about 30% is dissipated in atom displacements [Hof98]. The ion must dissipate the rest of this energy ultimately as phonons (heat). This whole process consists of three stages: (a) a collision stage of 10^{-13}s; (b) a thermalization stage of 10^{-12}s; and (c) a relaxation stage after 10^{-10}s. Process (b) and/or (c) allow the excess density to relax to zero, and cause a loss of sp^3 bonding at higher ion energies.

Consider an incident beam of flux F with a fraction ϕ of energetic ions of energy E_i. Let a fraction f of the energetic ions penetrate the surface. The non-energetic fraction of atoms or ions $(1 - f\phi)$ will just stick on the outer surface. Some of the penetrating ions

will relax back to the surface. This flux is proportional to a driving force, the fraction of interstitials below the surface, n. Thus, in the steady state, we write that the fraction of ions remaining at interstitial sites to give densification as $n = f\phi - \beta n$, where β is a constant. This gives

$$n = \frac{f\phi}{1+\beta} \tag{2.2}$$

Thus, a fraction n of the beam becomes sub-planted inside the film and a fraction $1 - n$ is left on the surface, as sp^2 sites. The sub-planted fraction creates a density increment of

$$\frac{\Delta\rho}{\rho} = \frac{n}{1-n} \tag{2.3}$$

which gives

$$\frac{\Delta\rho}{\rho} = \frac{f\phi}{1-f\phi+\beta} \tag{2.4}$$

where ρ is the density of sp^2 carbon, $\Delta\rho$ the density increase.

Figure 2-5 shows that penetration can occur in two ways, either directly or indirectly by knock-on. Only knock-on penetration occurs for the case of ion assisted deposition. The penetration probability can be estimated as a function of ion energy and follows roughly,

$$f = 1 - \exp\left(-\frac{E-E_p}{E_s}\right) \tag{2.5}$$

where E_p is the penetration threshold, and E_s is a constant (spread) parameter.

The first numerical models assume that relaxation occurs in the thermal spike stage of $\sim 10^{12}$ s [Y44]. This gives a relaxation rate of $\beta \approx 0.016\ (E_i/E_0)5/3$, with E_0 a diffusion activation energy, and

$$\frac{\Delta\rho}{\rho} = \frac{f\phi}{1 - f\phi + 0.016(E_t / E_0)^{5/3}} \tag{2.6}$$

This equation gives a good representation of the variation of density or sp^3 fraction for ta-C [Fal93]. This value is consistent with the thermal stability of deposited ta-C up to 1000K. The increasing sp^3 fraction at low ion energy is controlled by the penetration probability *f*, and the decline in sp^3 fraction at high ion energy is controlled by the relaxation. In addition, this model is well supported by the result that the increase of sp^2 in the ta-C films was occurred by increasing the deposition temperature of substrate during the deposition process [Chh97].

Amorphous carbon films are suitable as wear resistant coatings or protective over coatings because of their high hardness, high wear resistance, low coefficient of friction and chemical inertness [Gor94, Pan95, Pap94]. However, the application of these coating is restricted due to the problems of achieving a sufficiently high adhesion due to high residual compressive up to 12 GPa, which also limits the film thickness. There have been several reports of successful applications of amorphous carbon films [Bhu99, Gog01]. Among them commercial example was the DLC coating of razor blades [Dec97]. Here, DLC (ta-C) films with at least 40% sp^3 carbon bonding were deposited by arc evaporation with a hardness of 45 GPa and a modulus of 400 GPa. In this example, no intermediated layers are used for the ta-C adhesion but the sample bias is held initially at high voltage (2kV) presumably to reduce the compressive stress in the initial layer, and subsequently reduced to approximately 100V.

Thin DLC films have also been investigated for use as slider overcoats on read-write head and magnetic hard disks in high areal density magnetic recording [Bhu99]. In the case of sliders, thin films 1.5 – 7 nm thick, were found to have satisfactory

tribological properties for magnetic recording applications. Hard drive coatings are typically 3 – 7 nm thick, require a uniformity of 10% or better over 10 cm and a high deposition rate (~ 4 s both sides). The coatings are necessary as a protective layer between the slider and disk must be thin enough in order to achieve sub-10 nm working distances for storage densities of 15 Gb/cm^2 [Bhu99].

Table 2-1. The bond length and energy of various carbon couples.

Bond	Hybrid Type	Bond Length (nm)	Approximate Bond Energy*		
			kJ/mole	kcal/mole	eV**
C-C	sp^3	0.154	370	88	3.82
C=C	sp^2	0.134	680	162	7.41
C≡C	sp^1	0.121	890	213	9.24
C-H	sp^3	0.109	435	104	4.51
C-O	sp^3	0.14	360	86	3.73
C-N	sp^3	0.15	305	73	3.17

* Energy required to break one mole of bonds.
** 1 J = 0.2389 cal = 6.242×10^{18} eV.

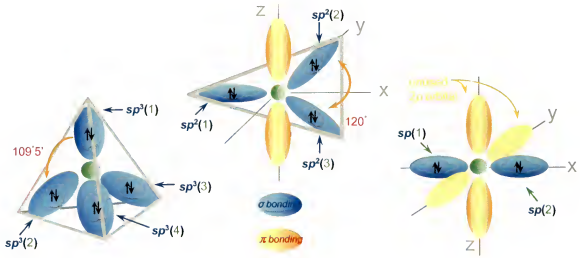

Figure 2-1. Different types of carbon bondings: (a) sp^3, (b) sp^2, and (c) sp^1 hybridizations.

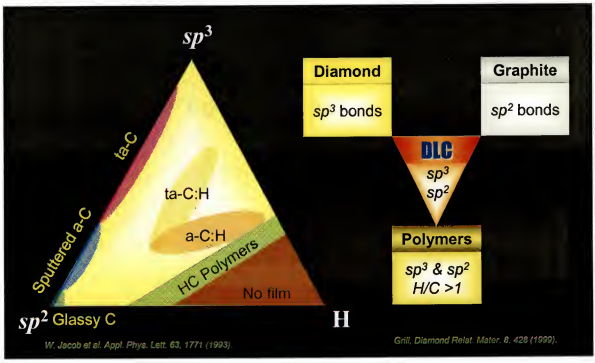

Figure 2-2. A ternary phase diagram of bonding in amorphous carbon-hydrogen alloys.

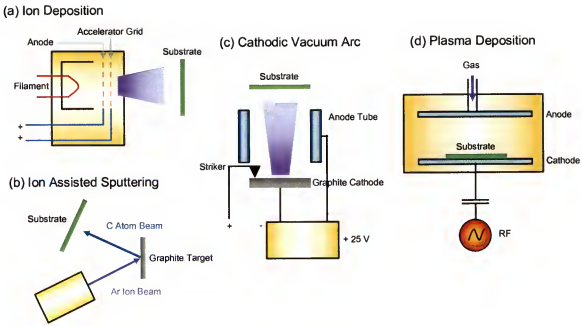

Figure 2-3. Schematic of various deposition systems for amorphous carbon films.

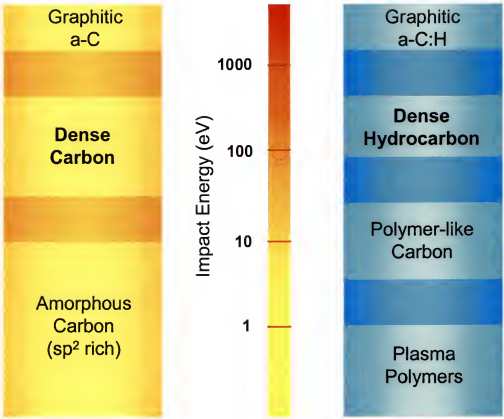

Figure 2-4. Schematic of different bonding characteristic on ion energy during deposition of amorphous carbon films.

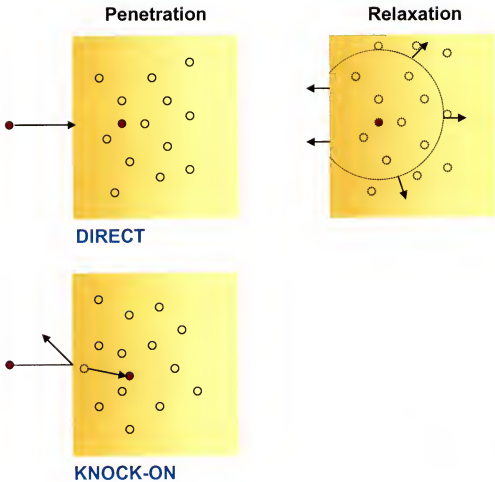

Figure 2-5. Schematic of the basic processes in subplantation model: direct penetration, penetration by knock-on of a surface atom, and relaxation of a densified region.

CHAPTER 3
GROWTH AND CHARACTERIZATION OF LOW STRESS DIAMOND-LIKE CARBON FILMS BY A MULTI-CYCLE PROCESS

3.1. PLD Grown Diamond-like Carbon Films

Diamond-like carbon (DLC) is in the form of either tetrahedral amorphous carbon (ta-C) or hydrogenated amorphous carbon (a-C:H) [Erd01, Rob02]. Due to their unique properties such as high hardness, low friction, chemical inertness and optical transparency, DLC films are used in wide areas of industrial applications such as protective coatings, optical windows, magnetic storage disks and cutting tools [Gri99]. The mechanical hardness and thermal stability of ta-C films with high sp^3 contents are superior to those of a-C:H films. This is attributed to higher degree of C-C network and less hydrogen atom content in ta-C structure [Rob02].

Pulsed laser deposition (PLD) has been shown as one of the promising methods to deposit unhydrogenated DLC films. PLD produced ta-C films contain relatively high contents of sp^3 hybridized carbon atoms [Tab99, Yam98]. However, coating delamination is frequently observed due to the high intrinsic stress generated during the deposition process. This high residual stress is attributed to the so-called *growth-induced stress* developed during the coating condensation process [Rot87]; and it strongly depends on the deposition process as well as the process parameters. This high stress limits the thickness of DLC coating, often to less than 1 μm thick. It also affects the adhesion of the film and puts the restriction upon the technical applications of DLC. For the successful application of DLC films as coating materials, the produced DLC coating

layers must adhere well to the substrate materials and the adhesive forces must overcome the high internal stresses that would otherwise cause film delamination and coating failure [Erd01].

Several approaches have been made to overcome these problems. Incorporation of foreign elements into DLC films has been extensively studied to produce stress-released DLC films with enhanced adhesion onto various kinds of substrates. Wood et al. reported a study of nitrogen-doped DLC films deposited by RF plasma decomposition of a hydrocarbon vapor and N_2 mixtures, in which both the compressive stress and the hardness were reduced by a similar factor with nitrogen addition [Woo95]. The stress release mechanism was explained by the reduction in average coordination number in DLC films due to the nitrogen incorporation [Fra92]. It is also reported that DLC films containing metal (W, Cr, Ti, etc.) indicate low internal stress and high toughness, and have been used as modified forms of DLC films in some applications [Gri93]. However, there are still controversial issues, regarding the different approaches of understanding and interpreting of the mechanism and results in each study. Sometimes even similar approaches resulted in opposite trends [Woo95, Smi01]. Therefore, more profound studies will be required for the further understanding of the stress release mechanism and successful applications.

In this study, DLC films will be deposited by a multi-cycle process of PLD to lower the intrinsic compressive stress, while minimizing the loss of sp^3 network. It has been reported that the thin surface layer of PLD produced DLC film is sp^2-rich, compared to underlying layers [Dav98, Xu98, Sie00]. This is due to the lower energy of surface plasmon compared to that of bulk part [McK91, McK96]. Multi-cycle deposition will

allow the formation of sp^2-rich surface layer at the end of each deposition cycle. The formation of this low-density intermediate layer is expected to help releasing the high intrinsic stress compiled during deposition process.

3.2. Experimental Procedures

3.2.1. Film Synthesis

Figure 3-1 shows the schematic diagram of the PLD system used for the deposition of DLC films. KrF excimer laser ($\lambda = 248$ nm; $\tau = 25$ ns) was used to ablate the target material at a repetition rate of 5 Hz. Si (100) wafers were used as substrate material for the growth of DLC. Before loading into the chamber, the substrate was ultra-sonically cleaned with acetone and methanol, sequentially. A cleaned Si piece (1.5 cm x 1.5 cm) was mounted on a substrate holder located 4 cm away from a hydraulic compressed graphite target of very high purity (99.99%). All depositions were performed at room temperature in a high vacuum of better than $\sim 10^{-6}$ Torr. The focused laser beam was incident at an angle of 45° on the target. The target has rotational motion during the deposition process to ensure a uniform erosion pattern upon the target surface. Different laser energy densities (1 J/cm^2 to 7.2 J/cm^2) were used to produce DLC with different sp^3 contents. DLC films were deposited by a multi-cycle process (total 10 times repetition of 30 sec deposition followed by 30 sec relaxation period) to relieve the high internal stress, which is known to develop during the coating condensation process [Gri99, Rob02]. Single-cycle PLD process was also used to produce highly-stressed DLC to compare the results.

3.2.2. Film Characterization

An α-step profilometer (KLA-Tencor α -step mechanical stylus profilometer) was used to measure the thickness of DLC films. For this measurement multiple steps were

made on a dummy wafer which was also conventionally cleaned and mounted on the substrate holder. The thickness of the deposited layers varied between 0.1 to 1 μm. Stress measurements were done by the well-known radius of curvature technique with Stoney's equation. Raman spectroscopy (Reinshaw Rama scope-1000) was used to analyze the small dimensional carbon network in the films. The laser wavenumber used for the Raman measurement was 514 nm. The composition of film was estimated by Auger electron spectroscopy (Perkin Elmer PHI 5100 ESCA System). X-ray photoelectron spectroscopy (Perkin Elmer PHI 600 Scanning Auger Multiprobe) was also used to analyze the composition of films, and to confirm the bonding structure. Transmission Fourier transform infrared (IR) spectroscopy (Nicolet MAGNA 760 FTIR Bench), equipped with a conventional DTS detector in the wavenumber range of 4000 – 600 cm^{-1} was used to reveal carbon bonds in the films. FTIR spectra were obtained from pellets containing 1 mg sample in approximately 100 mg potassium bromide (KBr). Atomic force microscopy (AFM: NanoScope® IIIa with Dimension™ 3100 Controller) was used to acquire surface morphology and RMS roughness of DLC film. Optical microscopy (Olympus BX 60) with reflection mode was also employed to observe the highly-stressed DLC films. The images from microscopy were acquired digitally (MTI 3CCD Camera) by Scion image software (Scion corporation).

3.3. Results and Discussion

Figure 3-2 shows the typical Raman spectra of DLC films deposited by PLD at different laser energy densities, varying from 1.0 J/cm^2 to 7.2 J/cm^2. Raman spectroscopy is a relatively simple and non-destructive analysis tool to characterize the structural changes of carbon materials. It has been thus widely used to analyze the structural

variation in amorphous carbon films such as hydrogenated amorphous carbon (a-C:H), tetrahedral amorphous carbon (ta-C) and amorphous carbon nitride (CN_x) films [Yos89, Pra96, Sch96]. As it can be seen in Fig. 3-2, there are significant changes in the peak shape and the intensity of Raman spectra. These spectral changes indicate that the PLD can produce DLC of various structures. The two films prepared at low laser energy densities show very broad Raman spectra with very low intensities (Fig. 3-2 (a) & (b)). This is because these films show strong fluorescence, which often appears in films with polymeric structures. In case of the films deposited with laser fluences higher than 2.4 J/cm^2, Raman spectra exhibit DLC characteristic with a prominent peak located at ~1500 cm^{-1} (Fig. 3-2 (c) – (f)). Raman spectra of DLC films show more symmetric and narrower shape when compared to those of polymeric carbon films. Proper deconvolution process is required for more accurate observation. Figure 3-3 shows a typical curve fitting of Raman spectrum of DLC film using two Gaussian curves. In general, the Raman spectra of amorphous carbon films consist of a broad peak at ~1550 cm^{-1} (G-peak) and a shoulder at ~1350 cm^{-1} (D-peak) [Tam94]. It is well known that the G-peak originates from E_{2g} phonon among the zone center modes of graphite sheet. On The other hand, D-peak intensity is closely related to the sp^2 cluster size, although the exact origin of D-peak is still in controversy [Cue94]. It is important to note at this point that the G-peak, being a bond stretching mode of C=C dimer, would occur in both aromatic sp^2 ring and sp^2 chains of carbon atoms, while the D-peak would only be detected in the presence of clusters of aromatic sp^2 rings. Therefore, the stronger the D-peak component in the Raman spectra, the more aromatic sp^2 rings present in DLC film, exhibiting more graphite-like structure. Details will be explained below. Figure 3-4 shows Raman spectra

fitting curves of DLC deposited at four different laser energy densities. Each peak shows different fitting result. The ratio of relative intensity of D- and G- peak (I_D/I_G) is a very important parameter, which gives the information on the microstructure of DLC films. I_D/I_G is a measurement of the degree of disorder in DLC, and this ratio can be used as an indicator of the number and the size of sp^2 bonded nanoclusters (a few nanometers) of aromatic ring in amorphous carbon films. In general, the I_D/I_G ratio decreases with the increase of sp^3/sp^2 bond fraction in DLC films [Fer00, Rob02]. DLC deposited at 2.4 J/cm^2 exhibited an I_D/I_G value of 1.16 (Fig. 3-4 (a)). This relatively high value falls rapidly to 0.87 for the DLC deposited at 4.0 J/cm^2 (Fig. 3-4 (b)). This decrease of I_D/I_G implies the increase of sp^3 C hybridization content in DLC deposited at 4.0 J/cm^2. Indeed, XPS result shows the enhanced sp^3 bonding content from DLC deposited at 4.0 J/cm^2 (24%) when compared to DLC at 2.4 J/cm^2 (16%) (Fig. 3-13). The Raman spectra of DLC films deposited at higher energy densities show the same trend, i.e. I_D/I_G continuously decreases with increasing laser fluence (Fig. 3-4 (c) & (d)). In this study, higher laser fluence produces DLC film with a higher sp^3 fraction, which gives more diamond-like characteristic to the deposited film. This will be confirmed with the XPS and the nano-indentation results later in this chapter and in Chapter 6, respectively.

Figure 3-5 shows the variation of I_D/I_G and G-peak width estimated from the Raman spectra of DLC films in Fig. 3-4. As the laser energy density increased from 2.4 J/cm^2 to 7.2 J/cm^2, the I_D/I_G intensity ratio decreased from 1.16 to 0.61 and the G-peak width increased from 184 cm^{-1} to 206 cm^{-1}. Again, the continuous reduction of I_D/I_G value implies that the DLC film deposited at the highest energy density (7.2 J/cm^2) possess the highest sp^3 content, along with highly distorted sp^2 rings. The Raman G-peak

width is another important parameter to estimate the homogeneous disorder and the bond angle distortions within the carbon network. This value reaches a maximum in the most 'diamond-like' DLC film, where the density, C-C (sp^3) bonding, mechanical hardness and stress all have a maximum [Gri99]. Therefore, the behavior of G-peak width which shows an opposite trend against that of I_D/I_G reconfirms that the DLC produced at 7.2 J/cm^2 shows the most diamond-like property.

When comparing the location of Raman peaks at 2.4 J/cm^2 and 7.2 J/cm^2, the G-peaks tend to shift downward from 1530 cm^{-1} to 1516 cm^{-1} and the D-peak also show the same behavior with varying its location from 1357 cm^{-1} to 1344 cm^{-1} (Figure 3-6). The downward shift of the G-peak and D-peak are attributed to the decrease of a graphite-like sp^2 bonded phase, and indicates a much higher percentage of sp^3 bonding in the films, and the films are more diamond-like. The results are in good agreement with the variation of mechanical properties of these films shown in chapter 6, and is consistent with previous study [Rob02] that the sp^3 bonded carbon clusters mainly control the mechanical properties such as hardness and Young's modulus [Rob94].

The atomic composition and contamination of the deposited films were estimated by Auger electron spectroscopy (AES). Figure 3-7 shows a typical Auger spectrum of DLC film. It can be clearly seen that a strong carbon peak is detected from the AES spectra with small contents of nitrogen and oxygen, probably contributed from sample and target material handling.

IR spectroscopy is another widely used technique to characterize the bonding types in DLC. The IR absorption consist of C-H stretching modes at 2800 – 3300 cm^{-1} and C-C and C-H bending modes below 2000 cm^{-1} [Rob02]. The features in the C-H IR modes

follow closely those of hydrocarbon molecules. The modes, particularly above 1340 cm^{-1} are quite localized, so that their wavenumbers can be assigned reliably by comparison to their values in molecules [Rob02]. Figure 3-8 shows a typical FTIR spectrum of DLC film. It has been popular to fit the C-H bands with Gaussian curves to derive sp^3 fractions. However, the bands can be broad and the centers can drift, so the decomposition of the C-H stretching modes into the individual band is not unique [Ris98]. Also, the oscillator strength of the various C stretching modes is not constant. Therefore, the IR stretching modes are not a reliable way to obtain sp^3 content. [Gri92]. Besides, FTIR analysis is more frequently adopted for the study of a-C:H films deposited by chemical vapor deposition system. On the other hand, X-ray photoemission spectroscopy (XPS) has been considered as a more proper technique to be used for determining the sp^3 content of DLC deposited by PLD.

XPS consists of measuring the shifts of core levels by X-ray photoemission. XPS is chemically specific as each element has its own core level. The shifts reflect the chemical bonding of each site. The largest shifts are caused by the Coulombic potential from ionic charge on adjacent atoms. For SiO_2, the Si-O bond is polar, and the Si 2p level is shifted by 4 eV from its position in Si. Therefore, Si sites with 1, 2, 3 or 4 oxygen neighbors can be resolved. Only small shifts occur in carbon, which is homopolar. A small shift (~0.9 eV) is observed between the C 1s core level of diamond and graphite. This is attributed to the slightly shorter bond length of the sp^2 bonds than the sp^3 bonds [Hae02]. Therefore, the sp^2 sites experience a slightly deeper potential than the sp^3 sites. This difference can be used to determine the relative amount of sp^2 and sp^3 sites in DLC [Par02, Rob02]. An advantage of XPS is that both the sp^2 and the sp^3 sites can be distinguished, and that their

weighting is same. However, core levels can be broadened by disorder more than the shifts between sp^2 and sp^3, so the deconvolution of overall core spectrum is required to separate the two levels and to derive the sp^3 fraction [Dav98, Hae02]. The XPS survey spectrum shown in Fig. 3-9 illustrates the sharp peak at ~284.5 eV representing the characteristic binding energy of core electrons emitted from the DLC film. The trace of O and N is probably due to the contamination of the film surface after exposure to air. In this study, XPS spectra were taken without an Ar^+ ion bombardment etching process because it is possible to destroy or at least influence the chemical bonding structure of DLC structures.

The sp^3 fraction of DLC film was deduced from XPS fitting for C1s core peak, consisting of peaks due to diamond (C_D), graphite (C_G), and C-O contamination phases (C_O) located at 285.2 eV, 284.4 eV, and 286.5 eV, respectively. The contribution of the background was approximated by the Shirley method. Figure 3-10 demonstrates the deconvoluted XPS C1s peak. Since the area of each peak is directly related to the concentration of corresponding phase, the sp^3 content can be estimated by taking the ratio of diamond peak area over the sum of diamond and graphite peak area [Mer98, Tay99].

Figure 3-11 shows the XPS fitting results from the multi-cycle deposited DLC films at four different energy densities. It can be clearly seen that the relative area of C_D and C_G changes depending on the laser fluence. As the energy density increases, the area under sp^3 peak also increases monotonically. On the other hand, the area of sp^2 peak decreases at the same time. The variation of sp^3 fraction is demonstrated in Fig. 3-12. As the laser fluence increases from 2.4 J/cm^2 to 7.2 J/cm^2, the sp^3 content in DLC film increases from 16% to 65%. This enhanced formation of sp^3 bonding at high laser fluence

can be explained by the well-known subplantation model [Rob02]. Ions with higher energy can penetrate the amorphous carbon surface with larger probability resulting in the increase of local density by occupying the subsurface interstitial sites. This will increase the amount of sp^3 configuration which can accommodate more number of atoms in the same volume [McK93]. However, ions of extremely high energy are known to cause a loss of sp^3 bonding due to thermalization and relaxation process [Gri99, Rob02], which did not happen in this study.

Smooth morphology and good film coverage are critical issues for the coating application of DLC. The surface properties of DLC films were investigated by AFM. AFM data provide information on the surface morphology with root mean square (RMS) roughness of DLC film. It is well known that the deposition of sp^3-rich film is associated with the internal subsurface growth of very smooth films, while the formation of sp^2-rich film is associated with the surface growth process characteristic of much rougher films [Lif95]. Figure 3-13 shows the two-dimensional surface morphologies of DLC films deposited at laser fluences between 2.4 J/cm^2 and 7.2 J/cm^2. DLC deposited at 2.4 J/cm^2 shows a rough surface covered with randomly distributed small particulates, along with large-clustered island features (Fig. 3-13 (a)). From the results of Raman (Fig. 3-4) and XPS (Fig. 3-11), it was confirmed that the formation of sp^2 graphitic structures is preferred at this low energy density. The rough surface observed at 2.4 J/cm^2 is probably due to the surface growth of sp^2 graphitic phases at this energy density. The large clusters observed on the surface might be the consequence of growing particles by negative ions in the plasma. Diamond-like carbon deposited at 2.4 J/cm^2 with high sp^2 content gives relatively high RMS value of 0.862 nm. The large clusters on the right side of the image

were excluded by selecting an area of ~2 μm^2 and calculating the RMS values from this selected area only. RMS roughness was measured from ten different locations to obtain the final average value. DLC deposited at 4.0 J/cm^2 still shows small particulates on the surface. However, the average particulate size is smaller when compared to that of DLC 2.4 J/cm^2 and they exist as small features rather than as large clusters. This is attributed to the reduced formation of aromatic sp^2 phase and increased sp^3 fraction at 4.0 J/cm^2. Also, the high laser energy enhances the dissociation and activation of particles in the plasma, resulting in only small and uniformly distributed particles on the surface. The RMS roughness shows a decreased value of 0.491 nm at this energy density. The similar trend is observed from the DLC deposited at 5.6 J/cm^2 and 7.2 J/cm^2 (Fig. 3-13 (a) & (b)). As the sp^3 fraction increases at high energy densities, the atomic density must be increased due to the increased accommodation in the film structure. This dense structure contributes to the low RMS value of DLC deposited at high laser fluence, along with better dissociation of particles in the plasma. The DLC film deposited at 7.2 J/cm^2 (sp^3% = 65%) shows smooth surface morphology with extremely low RMS value of 0.283 nm. Figure 3-14 shows three dimensional images of DLC films at different laser fluences. It can be easily seen that higher laser fluence produces smooth surface morphology with less particulates. Figure 3-15 shows the variation of sp^3 fraction and RMS roughness with the laser fluences. It is clear that DLC with lower sp^3 content, i.e. higher sp^2 content, shows larger RMS value.

As mentioned above, the conformal film coverage is another important factor to consider for the DLC coating applications. All DLC films shown in Fig. 3-13 and 3-14 were deposited by the multi-cycle process. Although DLC films deposited at different

energy densities showed quite a variation in roughness values, all films deposited by the multi-cycle process did not show any sign of film buckling, which is a well known problem of DLC due to the high internal compressive stress accumulated during the coating condensation process [McK91, Wei99]. However, the buckling phenomena occurred in the DLC films deposited by a single-cycle process, even though the total net deposition time was same, namely 5 minutes. The residual stress (σ) in each film was determined by the radius of curvature technique. Prior to deposition, the curvature radius of bare Si substrates (R_0) was evaluated by a surface profiler. The sample after deposition was also measured at the same reference points to obtain the radius of curvature (R). Combined with the measured film thickness, the stress in the film (σ_s) was then given by the well-known Stoney's equation [Che99].

$$\sigma_s = \frac{E_s}{6(1-\nu_s)} \frac{t_s^2}{t_f} \left(\frac{1}{R} - \frac{1}{R_0} \right) \tag{3.1}$$

where E_s (130 GPa), ν_s (0.26), and t_s are the Young's modulus, Poisson ratio, thickness of substrate and t_f is the film thickness.

The residual stress of amorphous carbon films are compressive [Che99, Rob02]. The compressive stress values measured from the partially delaminated DLC deposited by the single cycle process at 6.4 J/cm^2 are ranging between 5.6 and 8.3 GPa. On the other hand, DLC films deposited by the multi-cycle process show lower stress values of only ~3 GPa. Figure 3-16 shows the various types of the buckling patterns observed with optical microscopy. Mountain-looking patterns, as well as the frequently reported sinusoidal shaped buckling result in coating failure of DLC films.

There has been fundamental issue to produce high quality DLC with high fraction of sp^3 bondings, since hardness, Young's modulus, and the stress of DLC all tend to be proportional to each other [Tam95]. The stress of the film reaches its maximum value when the hardness of DLC is maximized. Therefore, maximizing the hardness of DLC without buckling will result in minimizing the coating thickness. A large effort has been made to maximize the adherent film thickness, including the insertion of carbide-forming adhesion layers of Si, Cr, or W [Ugo90, Ant97], the use of multi-layers [And97], alloying other elements, such as N, Si, or metal [Mem86, Ogu91], etc.

In this study, the multi-cycle deposition process has been introduced to produce DLC films free of stress-induced coating failure. It has been known that the subplantation growth mechanism enables the PLD produced DLC possess a surface plasmon of lower energy than the bulk plasmon [Mck91, Mck96]. This implies PLD deposited DLC will have a thin surface layer of lower density than bulk portion. The existence of sp^2-rich, low density layer was proved by other studies. The spatially resolved cross-sectional electron energy loss spectroscopy (EELS) showed the variation of atomic density and sp^3 fraction of DLC film. Both values suddenly decreased at just below the surface layer. More interestingly, the density drop was observed in the middle of DLC layer, where the deposition process was interrupted [Dav93, Dav98, Xu98]. Also high resolution transmission electron microscope (TEM) study reported the existence of low density layer near the surface of DLC film [Sie00]. They found the low density layer of 0.5 – 2 nm thickness at the surface of PLD grown DLC, suggesting that the layering is an intrinsic property of the deposition mechanism [Sie98, Rob02]. These results give an idea that by depositing DLC with a multi-cycle process, it can be possible to form low density

layer at each period. This intermediate layer will help to relax stress developed during the subplantation growth mode and increase the maximum coating thickness without film delamination.

Figure 3-17 shows the residual stress and the sp^3 content of the multi-cycle deposited DLC films at different laser fluences. Compared to the single-cycle deposited DLC, which showed large stress values of higher than 5.6 GPa, the multi-cycle processed films show residual stress values between 2.68 GPa and 3.37 GPa. The good film coverage observed by AFM (Fig. 3-13 & 3-14) supports these low stress values of the multi-cycle deposited DLC coatings.

Figure 3-18 shows the deconvoluted XPS C1s peak of DLC deposited by the single-cycle process at the energy density of 6.4 J/cm^2. The calculated sp^3 content in this structure was 63%, which was slightly lower than that of DLC produced by the multi-cycle process at 7.2 J/cm^2 (65%:Fig. 3-11 (d)). It is hard to directly compare the sp^3 fraction of both films because each film was deposited at different laser energy densities. However, the fact that sp^3 content of the multi-cycle deposited DLC at 5.6 J/cm^2 being only 34% (Fig. 3-11 (c)) gives an insight that the single-cycle deposition can produce DLC of higher sp^3 content than the multi-cycle process at the same laser fluence. This is probably attributed to the uninterrupted subplantation growth mode, allowing the continuous formation of sp^3 network in the single-cycle process. Unfortunately, this over-constrained structure induces a high level of internal compressive stress, resulting in severe buckling phenomena (Fig. 3-16). As mentioned above, one of the most important considerations in industry application is to produce DLC coatings without film delamination. Therefore, the multi-cycle process can be considered as a good choice to

produce high quality DLC without coating failure. In addition, the systematic nano-indentation measurements will reveal that the hardness and elastic modulus values of DLC deposited by single-cycle and multi-cycle process show only slight differences (Chapter 6).

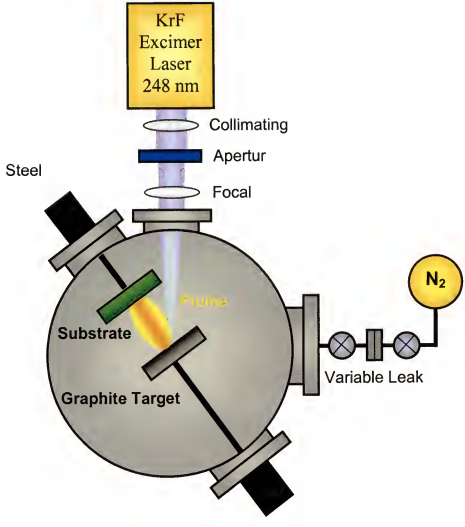

Figure 3-1. Schematic of the PLD chamber used for DLC deposition.

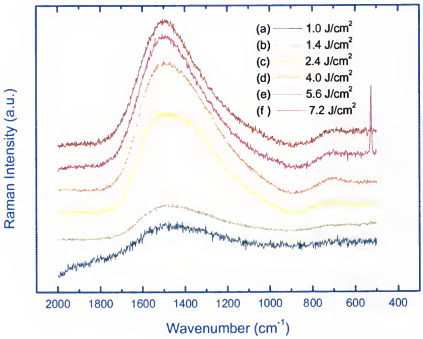

Figure 3-2. Various Raman spectra of PLD deposited DLC at different laser fluences.

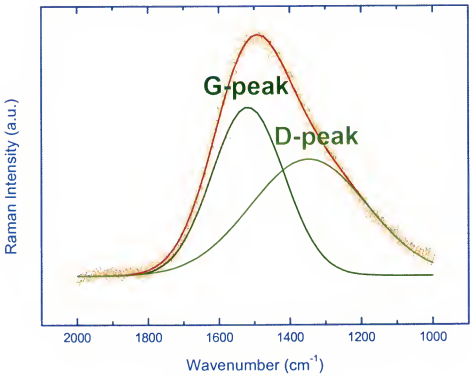

Figure 3-3. A fitting example of DLC Raman spectrum with D-peak (~1350 cm^{-1}) and G-peak (~1550 cm^{-1}).

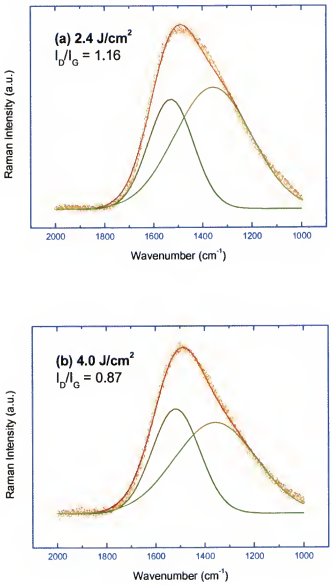

Figure 3-4-1. Fitted Raman spectra of DLC deposited at (a) 2.4 J/cm^2 and (b) 4.0 J/cm^2.

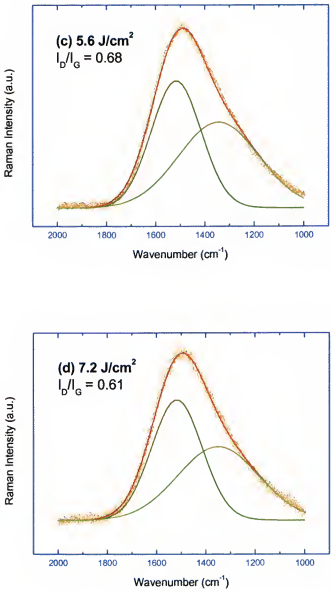

Figure 3-4-2. Fitted Raman spectra of DLC deposited at (c) 5.6 J/cm^2 and (d) 7.2 J/cm^2.

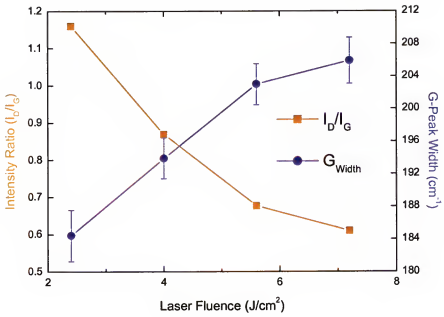

Figure 3-5. The dependence of I_D/I_G ratio and G-line width on the laser fluence.

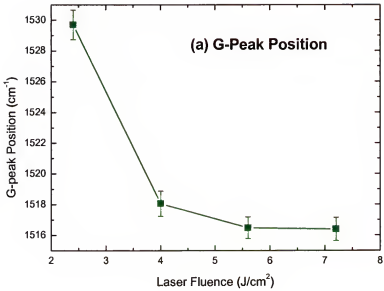

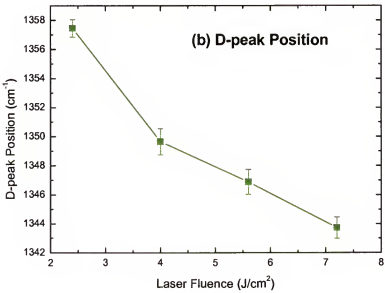

Figure 3-6. The dependence of G-peak and D-peak positions on the laser fluence.

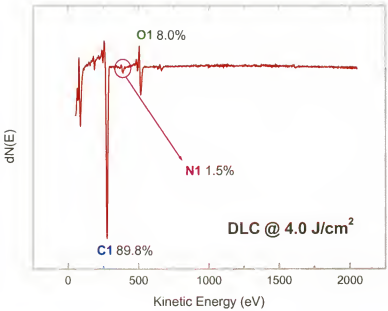

Figure 3-7. A typical Auger spectrum of DLC deposited by PLD process.

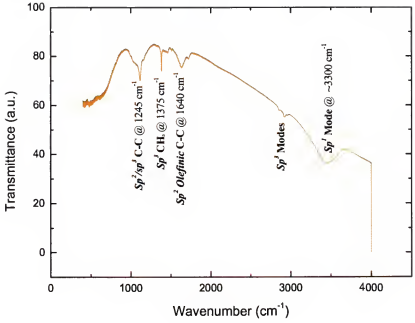

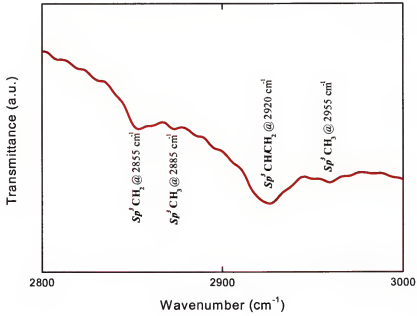

Figure 3-8. An example of the IR stretching of DLC deposited at 4.0 J/cm^2.

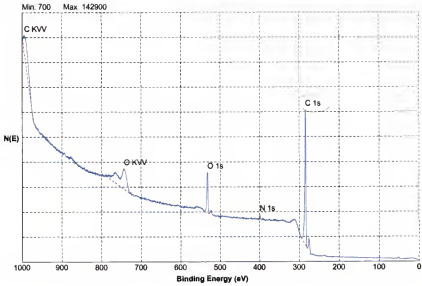

Figure. 3-9. A XPS survey scan of DLC deposited at 4.0 J/cm^2.

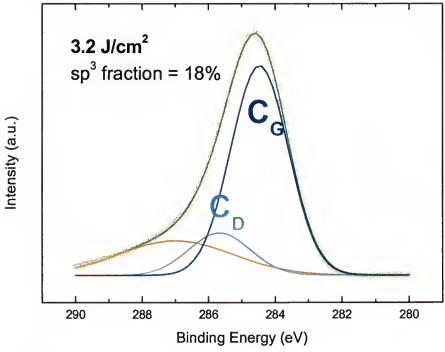

Figure 3-10. A fitting example of the XPS C 1s peak of DLC deposited at 3.2 J/cm^2.

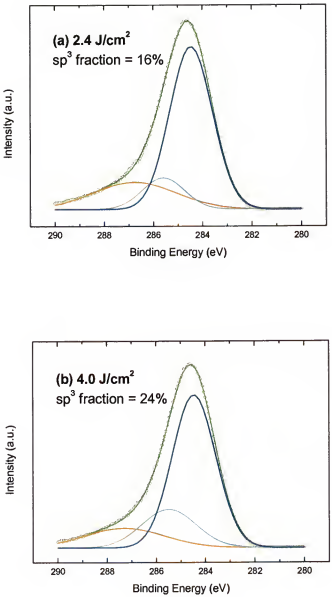

Figure 3-11-1. XPS C 1s core peak of DLC deposited at (a) 2.4 J/cm^2 and (b) 4.0 J/cm^2.

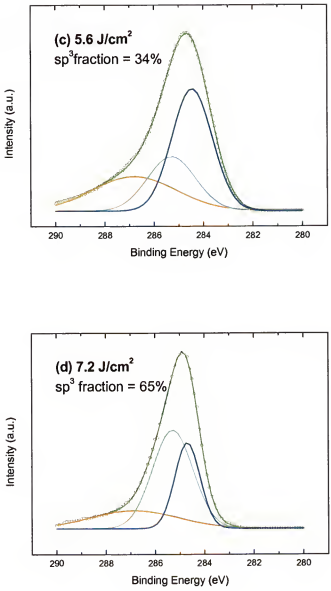

Figure 3-11-2. XPS C 1s core peak of DLC deposited at (c) 5.6 J/cm^2 and (d) 7.2 J/cm^2.

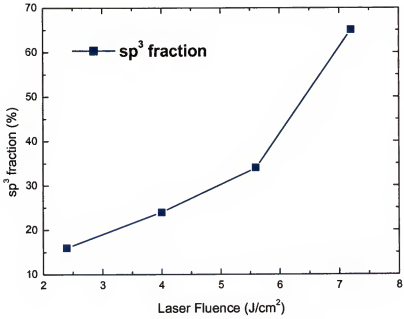

Figure 3-12. Variation of sp^3 content in PLD deposited DLC with laser fluence (J/cm^2).

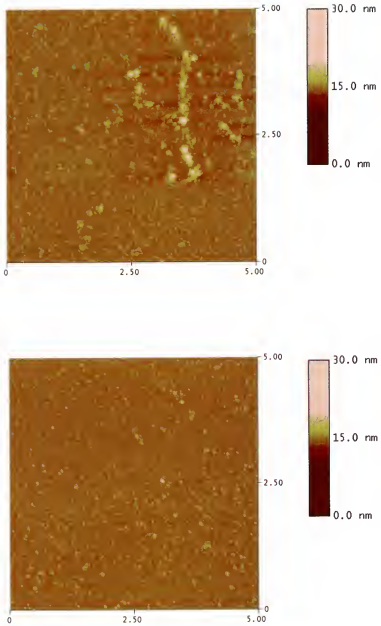

Figure 3-13-1. 2-D AFM images of DLC deposited at (a) 2.4 J/cm^2 and (b) 4.0 J/cm^2.

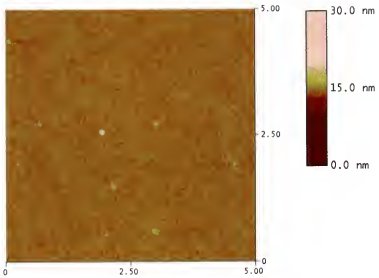

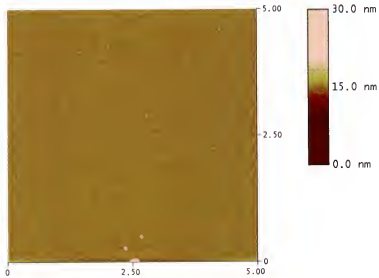

Figure 3-13-2. 2-D AFM images of DLC deposited at (c) 5.6 J/cm^2 and (d) 7.2 J/cm^2.

RMS = 0.862 nm

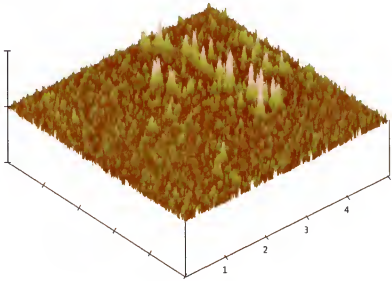

RMS = 0.491 nm

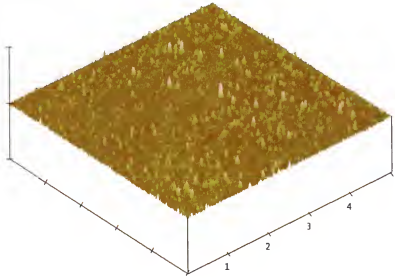

Figure 3-14-1. 3-D AFM images of DLC deposited at (a) 2.4 J/cm^2 and (b) 4.0 J/cm^2.

RMS = 0.397 nm

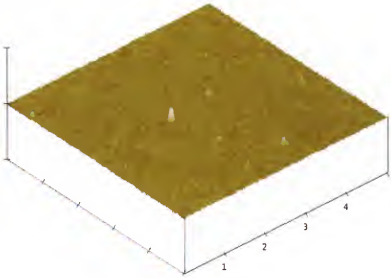

RMS = 0.283 nm

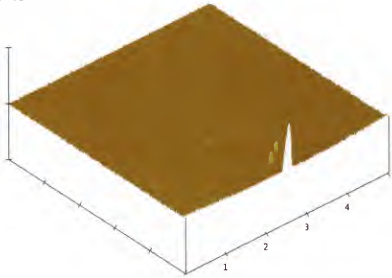

Figure 3-14-2. 3-D AFM images of DLC deposited at (c) 5.6 J/cm^2 and (d) 7.2 J/cm^2.

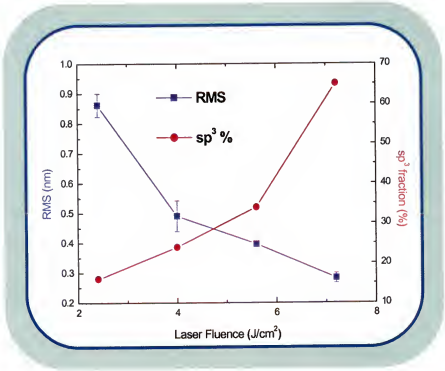

Figure 3-15. Dependence of (a) RMS roughness and (b) sp^3 fraction on the laser fluence.

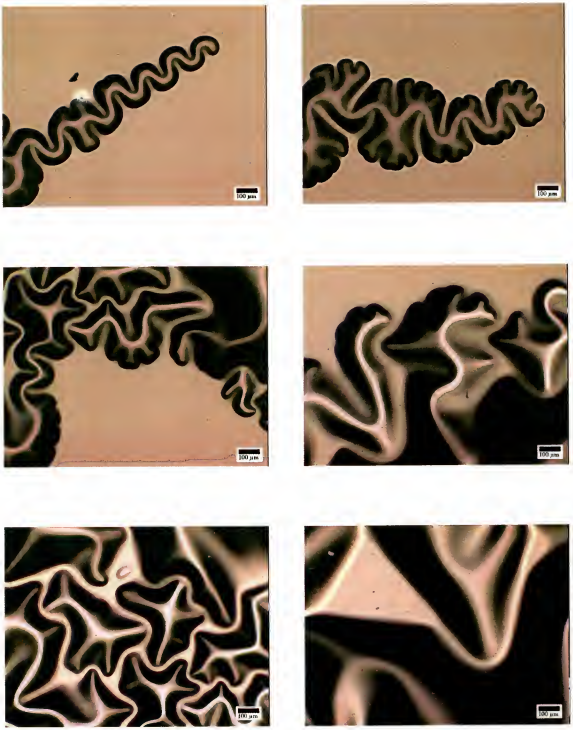

Figure 3-16. Optical images of the buckling patterns on the highly stressed DLC films

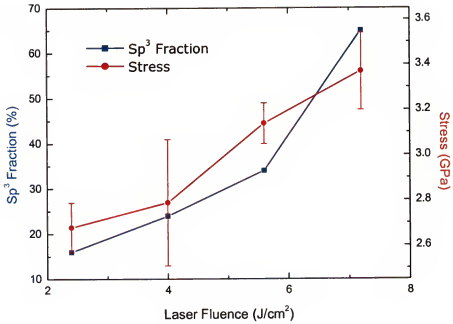

Figure 3-17. Dependence of the residual stress and the sp^3 contents of the multi-cycle deposited DLC films on the laser fluence.

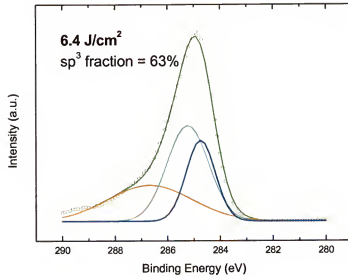

Figure 3-18. The fitted XPS C 1s peak of a highly stressed DLC by the single cycle PLD process.

CHAPTER 4
GROWTH AND CHARACTERIZATION OF AMORPHOUS CARBON NITRIDE FILMS WITH LOW NITROGEN CONCENTRATION

4.1. Amorphous Carbon Nitride Films

Ever since it was proposed that C_3N_4 could have a bulk modulus comparable to diamond, large efforts have been made to synthesize this material [Liu89, Liu90, Rob02]. There are two main requirements to get C_3N_4, which are the high nitrogen incorporation to reach the 4/3 stoichiometry, and the sp^3 bonded carbons to form a rigid network. In reality, both conditions are hard to achieve at the same time. Instead, amorphous carbon nitride (CN_x) films are usually produced [Muh99, Rie00]. The CN_x films contain relatively low nitrogen concentration of below 10%. Due to the low residual stress and similar properties with DLC, the CN_x films have been studied intensively for various coating applications [Hay00, Sil97, Sjo96, Tan98, Tet96, Wie01]. The small amount of nitrogen concentration modifies the graphitic structure of CN_x film. Nitrogen can stabilize the five-fold pyrrole ring since it has one more electron than carbon and now, therefore, gives the six π electrons needed for the aromatic stability. These rings can introduce a certain degree of warping in the graphitic layer, resulting in the changes in bond angle and length. This will lower the compressive stress in CN_x structure [Rob02]. Also, a reduction of the average coordination number is known to play an important role in releasing the internal stress of films.

Different types of deposition methods, such as sputtering [Sjo96, Tan98], ion beam assisted deposition [Alv98], nitrogen ion implantation [Lee97], cathodic vacuum arc

[Che99, Spa97], and plasma enhanced chemical vapor deposition [Che00] have been used to synthesize the CN_x thin films. Due to the high ion energy and the high sp^3 contents of produced films, PLD is one common method to deposit CN_x films [Che02a, Niu93, Zha01].

For the complete understanding of CN_x materials, which is essential for tailoring of their properties, it is important to know the detailed bonding configurations of carbon and nitrogen atoms in their structure. Although there have been numerous publications on this subject [Che02a, Che99, Wie01, Zha01], there are still considerable confusions on how spectroscopic data should be interpreted. This complexity is mainly attributed to the fact that the vast majority of films exhibit non-crystalline structures, and therefore, crystallographic methods have not been useful for the structural characterization of CN_x films. In this study, a systematic study of CN_x films by various techniques, such as AES, XPS, Raman spectroscopy will be performed to gain an insight into their local bonding structure and relate it to the film properties, including the low residual stress. The morphologies of various CN_x films will be closely observed with AFM.

4.2. Experimental Procedures

4.2.1. Film Synthesis

The CN_x films were deposited by PLD onto Si (100) substrates. The substrate was ultra-sonically cleaned in acetone and ethanol baths before being loaded into the deposition chamber. The target was 2-inch diameter graphite disk of 99.99% purity, separated 4 cm from Si (100) substrate. After the base pressure of ~ 10^{-6} Torr was achieved, the process gas (N_2 of 99.999% purity) was introduced into the chamber through a mass flow controlling system until the desired pressure was established (*N1*: 5×10^{-2} Torr, *N2*: 1×10^{-1} Torr, and *N3* = 5×10^{-1} Torr). A KrF excimer laser ($\lambda = 248$

nm; $\tau = 25$ ns) was used to ablate the graphite target. The pulse energies of 300 – 900 mJ were selected to produce 2.4 – 7.2 J/cm^2 laser fluences on the target after focusing. All depositions were performed for 5 minutes at 5 Hz of repetition rate.

4.2.2. Film Characterization

The AES spectra were recorded using electron beam with the incident energy of 5 keV to examine the atomic composition of CN_x films. A micro-Raman spectrometer (Reinshaw Rama scope-1000) was used to acquire the structural information of CN_x films. Excitation was provided by the 514 nm line of a Kr ion laser (~100 μ W in the < 2 μ m laser spot). Meanwhile, the chemical compositions and various bonding configurations were determined by XPS (Perkin Elmer PHI 5100 ESCA System) using a MgK$_\alpha$ ($h\nu$ = 1253.6 eV) X-ray source. To avoid damaging the bonding structure of CN_x, all films were analyzed without sputter cleaning. The nitrogen content was calculated from the area integration of C 1s and N 1s peaks using the sensitivity factors of 0.250 and 0.420 for C 1s and N 1s peaks, respectively. Film thickness was measured by KLA-Tencor α-step mechanical stylus profilometer. Compared to the DLC at the same laser fluence, the thickness of CN_x was thinner, and the difference became larger at higher nitrogen partial pressure (NPP). The thickness values were ranged between 0.3 and 0.6 μm. Stresses of films were also measured by the radius of the curvature technique using the profilometer and Stoney's equation. The surface morphology and RMS roughness of CN_x were obtained by the contact mode AFM of NanoScope® IIIa with Dimension™ 3100 Controller.

4.3. Results and Discussion

Figure 4-1 demonstrates the variation of nitrogen contents of CN_x films at different laser fluences measured by XPS and AES. There is a little difference between the results of each analysis technique. Nitrogen concentrations acquired from XPS results show slightly higher values than those from AES results within allowable error range. In both techniques, the nitrogen content in CN_x film increases as the laser fluence increases. During the deposition of CN_x films, an interaction between the incident laser and the target material forms isothermally expanding plasma composed of electrons, atoms, ions, molecules, and clusters. Increasing laser fluence will result in the enhancement of ion densities and their energy in the plume [Koi99]. This will increase the ionization of N_2 molecules due to the collision of energetic ions with N_2 molecules, and result in the increase of the nitrogen incorporation at high laser fluence.

On the other hand, the effect of NPP on the nitrogen content of CN_x film is demonstrated in Fig. 4-2. All films were deposited at 5.6 J/cm^2, but with different NPP conditions. Both AES and XPS results show that the nitrogen content in CN_x film increases at high NPP, indicating that nitrogen was more effectively doped into the amorphous carbon structure during the deposition process at higher NPP. However, the increment of nitrogen in CN_x gradually decreases. At 500 mTorr (which is not shown in Fig. 4-2), the amount of nitrogen in CN_x shows only 7.1 at. % . This implies the existence of saturation stage of nitrogen incorporation in CN_x structure. As mentioned earlier, a high concentration of nitrogen has to be incorporated to achieve the hypothetic C_3N_4 structure. It is common to use additional energetic source, such as RF/Kaufman nitrogen atomic/ion beam sources [Gri99b, Jam97, Mer97] or a direct current (d.c.) glow

discharge apparatus [Che02a], to increase the nitrogen content in CN_x films. These sources can supply additional reactive nitrogen species during the deposition of CN_x.

In addition to measure the chemical composition of CN_x, the bonding configurations were also examined by XPS. The survey scan of CN_x revealed the existence of carbon, nitrogen and oxygen components in the film. Figure 4-3 shows the XPS C 1s spectra of CN_x films deposited at different laser fluences: (a) 2.4 J/cm^2 and (b) 5.6 J/cm^2. The NPP was fixed at *N1* (5×10^{-2} Torr) for both films. The C 1s spectra show a highly asymmetric peak at 284.6 eV towards higher binding energies. The asymmetric and broad feature of C 1s spectra indicates the existence of different bonding types in CN_x. By using the mixture of Gaussian and Lourentzian profiles, the C 1s spectra of CN_x films can be fitted well with following bonding structures: (1) a large component C1 at 284.3 eV refers to pure carbon sites including the C-C bonds; (2) a component C2 at 285.4 eV is related to the aromatic CN structures with three carbon atoms bonded to one nitrogen atom; (3) a component at 286.3 eV is due to the non-aromatic CN phase, the bonding between sp^3 C and nitrogen atom; and (4) a component at 287.4 eV corresponding to non-aromatic CN bonds with C atoms having two neighboring nitrogen atoms. To avoid complexity in the schematic, both non-aromatic components (3) & (4) are represented as one combined component, C3 at 287.2 eV, which refers to the non aromatic CN sp^1 and CN sp^3 components; (5) in addition, another C1s component, C4, located at binding energy of 288.8 eV is attributed to the C-O bonds [Fal93].

Accompanying behaviors of N 1s peaks are demonstrated in Fig. 4-4. As mentioned earlier, higher laser fluence produces the CN_x structure with higher nitrogen content (Fig. 4-1). Larger area of N 1s at 5.6 J/cm^2 shows the increase of nitrogen

incorporation at high energy density. The N 1s peak is deconvoluted into three peaks at 398.8 eV (N1), 400.1 eV (N2) and 401.6 eV (N3). These sub peaks are assigned as follows: (1) N1 represents the combined non-aromatic components of N-sp^3C (398.3 eV), and N-sp^1C (399.2 eV); (2) the nitrogen containing aromatic clusters (N-sp^2C) are responsible for the component N2; and (3) N3 results from trapped N_2 molecules or N-O in the films [Fal93]. The binding energy of different C 1s peaks and N1s peaks agrees relatively well with that of the referenced organic polymers.

The fitting results of XPS C1s (Fig. 4-3) and N1s (Fig. 4-4) spectra for CN_x deposited at 2.4 J/cm^2 and 5.6 J/cm^2 are summarized in Table 4-1(a) and (b), respectively. Slight decrease of the peak at 284.3 eV is observed (Table 4-1(a)). This may be due to the increase of nitrogen content in CN_x at high laser fluence, and fewer carbons are bonded to carbon atoms, resulting in the reduction of C-C peak. It is notable that the peak located at 286.3 eV shows a remarkable change. As mentioned earlier, this peak originates from the sp^3 carbon bonded to nitrogen. In chapter 3, DLC deposited at 5.6 J/cm^2 exhibits higher sp^3 fraction (34%) than the film deposited at 2.4 J/cm^2, which contains only 16% sp^3 configuration. Similarly, the enhanced sp^3 carbon fraction in CN_x provides the increased chance for nitrogen atoms to bond with sp^3 C atoms. As a result, the fraction of sp^3CN increases from 6.44% (2.4 J/cm^2) to 12.02% at 5.6 J/cm^2. At the same time, the contents of sp^2C=N and sp^1C≡N decrease at 5.6 J/cm^2, implying that the CN_x deposited at high laser fluence will show more diamond-like characteristic. The fitting results of XPS N 1s peak show similar trend with those of C 1s peak. Table 4-1 (b) indicates an increase in the content of nitrogen atoms bonded to sp^3 C, as well as a decrease in the content of nitrogen atoms bonded to other carbons, namely non-aromatic sp^1C and aromatic sp^2C.

Meanwhile, the effect of NPP on the nitrogen content and the bonding structure of CN_x is demonstrated in Fig. 4-5 and Fig. 4-6. These results are summarized in Table 4-2. The CN_x films were deposited at two different NPP conditions: *N1* = 5×10^{-2} Torr and *N2* = 1.5×10^{-1} Torr. Both films were deposited at 5.6 J/cm^2 to compare the influence of NPP only. The nitrogen contents show only a small difference at *N1* (N% = 5.9%) and *N2* (N% = 6.7%). However, the noticeable changes are observed in the bonding contents at 398.3 eV and 401.6 eV, which originate from the nitrogen bonded to sp^{3}C and to N/O atoms, respectively (Fig. 4-6). The fraction of sp^{3}CN decreases from 28.33% to 8.45% when NPP increases from *N1* to *N2*. On the other hand, the amount of nitrogen atoms bonded to nitrogen or oxygen increases almost three times at *N2* (Table 4-2(b)). This suggests that a large portion of increased nitrogen content in CN_x at *N2* exist without bonding to carbon species. The decrease of sp^{3}CN at *N2* is attributed to the reduced energy of plasma ionic species by the more frequent collision with N_2 molecules at high NPP [Gri99, McK93, Rob02]. The deconvoluted data of C 1s peaks also show similar results with N 1s peaks. The amount of sp^3 C bonded to nitrogen decreases about 47% by increasing the NPP from *N1* to *N2*. However, the portion of sp^2 CN bonding shows only slight change in both C 1s (C2) and N 1s (N2) fitted results. The data in Table 4-2 are schematically reproduced in Fig. 4-7. Again, the changes in fraction of sp^{3}CN bonding and non-CN bonding are apparent, indicating NPP is another crucial parameter to control the microstructure and properties of CN_x films

Raman spectroscopy is another useful tool to characterize the microstructure of amorphous carbon nitride films [Fer00, Rob94, Rod01]. Ferrari et al. reported that the visible Raman spectroscopy is 50 – 230 times more sensitive to the sp^2 sites because π

electrons are preferentially excited with visible photons [Fer00]. Figure 4-8 shows the Raman spectra of 1000 – 2000 cm^{-1} for CN_x films deposited at 2.4 J/cm^2 and 5.6 J/cm^2. The Raman spectrum of DLC film is also shown for the comparison. All spectra exhibit a broad asymmetric intensity distribution in the range of 1000 – 1700 cm^{-1} centered at ~ 1500 cm^{-1} with a shoulder band at ~1300 cm^{-1}. Main features of these spectra are the two broad peaks: the D-peak and G-peak, which are the characteristics of amorphous solid carbon materials. G-peak corresponds to the symmetric E_{2g} vibrational mode in graphite-like materials, while D-peak (or band) arises from the limitation in graphite domain size, induced by grain boundaries or imperfections, such as substitutional nitrogen atoms, or other impurities [Hel99]. Compared to the DLC spectrum, the CN_x spectra exhibit broader shoulder features at ~1350 cm^{-1}, giving more asymmetric characteristic in their shape.

In order to establish the detailed influence of laser fluence on the CN_x structure, Raman spectra were deconvoluted by the two peaks at approximately 1350 cm^{-1} (D-peak) and 1550 cm^{-1} (G-peak) [Che02b]. Figure 4-9 shows the fitted Raman spectra of CN_x deposited at (a) 2.4 J/cm^2 and (b) 5.6 J/cm^2, while NPP kept at *N1*. The proper curve fitting shows a minute difference between the two spectra, which could not be easily detected in Fig. 4-8. The CN_x deposited at 5.6 J/cm^2 shows slightly stronger D-peak, resulting in higher I_D/I_G ratio.

The variation of Raman parameters at different laser fluences are shown in Fig. 4-10. Several discrepancies are observed when compared to the result of DLC (Chapter 3). The I_D/I_G increases with laser fluence at a fixed NPP. This is attributed to the stabilization of aromatic sp^2 cluster by more nitrogen incorporation at high energy. Nitrogen also

increases the degree of disorder in the sp^2CN structure. For CN_x, some nitrogen atoms substitute with the carbon atoms constituting aromatic ring of the sp^2 graphite-like microdomain, that is, some of the sp^2 graphite-like microdomains change to the sp^2 pyridine-like microdomains or the five-fold pyrrole ring during the deposition [Tak97, Rob02]. Therefore, the sp^2C bondings in CN_x become more disordered and the D-peak (I_D/I_G) intensity becomes larger with increasing nitrogen content at higher laser fluence in spite of the higher sp^3 content. There was a similar report on the nitrogen content effect for the hydrogenated CN_x films [Rod01]. The up-shift of G-peak position and the broadening of D-peak at high laser fluence also reflect these structural changes in CN_x films (Fig. 4-10 (b)) [Kau89].

The CN_x film deposited at very high NPP (*N3*: 500 mTorr) shows Raman spectra of very unique shape (Fig. 4-11). The Raman results of CN_x deposited at lower NPP (*N1* & *N2*) are also shown in the figure. All films were deposited at 5.6 J/cm^2, leaving the NPP as the only effective process parameter. The separated D- and G-peak give entirely different feature. When considering the nitrogen content in this sample is only 7.1%, it is interesting that the Raman spectra show this huge difference. As mentioned earlier, Raman spectra of amorphous carbon structures are dominated by the scattering at sp^2 sites. Especially D-peak is only affected by the aromatic rings [Fer00, Rob02]. Therefore, this huge difference in Raman spectra is probably attributed to the enhanced formation of aromatic sp^2 clusters, and the aggravated disorder occurred at this high NPP. The Raman results of CN_x show that the sp^2 aromatic structures are intensified in CN_x compared to DLC, implying the CN_x films will exhibit lower stress and softer mechanical properties

than DLC films. Nanoindentation of *N3* CN_x shows the relatively low *H* (8.99 GPa) and E_r, (109.43 GPa).

The CN_x films show the lower residual stress than DLC films. The stress values calculated by Stoney's equation are ranging between 1.78 GPa and 3.01 GPa. All CN_x films exhibits good film coverage without any sign of buckling due to high stress. Concerning the effects of nitrogen incorporation on lowering the internal stress, it is worth to noting that nitrogen atoms admit a coordination number equal to 3 at most (sp^3 hybridized nitrogen). Therefore, the replacement of a carbon atom by a nitrogen necessarily implies a reduction of the average coordination number and hence of the degree of over-constraining, which is known to be the major stress source. This change in coordination number could be responsible for the internal stress reduction we observed. Also, the stress-relaxation can be explained by the stabilization and warping of sp^2 aromatic structure in amorphous carbon structure [Rob02]. Since nitrogen has one more electron than carbon, so that nitrogen in a five-fold pyrrole ring now gives the six π electrons needed for aromatic stability.

Morphologies and RMS roughness of CN_x films were observed with AFM. Three dimensional surface morphologies of *N1* CN_x films at 2.4 J/cm^2 and 5.6 J/cm^2 are shown in Fig. 4-12 (a) and (b), respectively. The CN_x at 2.4 J/cm^2 exhibits rougher morphology. The RMS roughness values of both CN_x films are 1.025 nm and 0.627 nm, respectively. Figure 4-13 shows the dependence of RMS roughness of *N1* CN_x films on the laser energy density. The RMS of CN_x shows a decreasing tendency at high laser fluence, which is similar to RMS variation of DLC. The high-energy deposited DLC showed smoother surface along with higher sp^3 content compared to the low-energy deposited

DLC, which consist of a larger amount of sp^2 aromatic phases (Chapter 3). Similarly, XPS revealed *N1* CN_x deposited at 2.4 J/cm^2 contains a lower fraction of sp^3CN, meaning the higher content of aromatic sp^2CN in this film (Table 4-1). Therefore, it can be concluded that the enhanced formation of sp^2 aromatic phase in *N1* CN_x deposited at 2.4 J/cm^2 resulted in the surface of higher RMS roughness. However, *N1* CN_x shows higher RMS values than DLC deposited at the same laser fluence. Also, CN_x deposited at higher NPP exhibits the rougher surface with more large particulates. It has been reported that the size of micro-particulate is influenced by the process pressure during deposition [Sae94]. In general, the size of a particulate increases at high ambient pressure due to the short mean free path, which results in the enhanced nucleation and growth of fine particulates before they reach the substrate. Fig. 4-14 shows AMF images of CN_x deposited at *N2*. Figure 4-15 shows the Raman spectrum of a particulate on the surface of *N2* CN_x deposited at 5.6 J/cm^2. It shows similar shape with the Raman of *N3* CN_x, but a very intense signal is detected at ~1580 cm^{-1}, which explains the graphitic nature of this particulate.

Table 4-1. Fitting results of XPS (a) C 1s (Fig. 4-3) and (b) N 1s (Fig. 4-4) spectra for CN_x films deposited at of 2.4 J/cm^2 and 5.6 J/cm^2.

	N content (at. %)	C 1s Binding Energy (eV)				
		284.3	285.4	286.3	287.4	288.8
2.4 J/cm^2	3.3	62.06	**8.47**	**6.44**	6.21	16.82
5.6 J/cm^2	5.9	60.64	**6.06**	**12.02**	3.95	17.34

	N content (at. %)	N 1s Binding Energy (eV)			
		398.3	399.2	400.1	401.6
2.4 J/cm^2	3.3	**16.99**	9.93	**63.99**	9.10
5.6 J/cm^2	5.9	**28.33**	7.91	**54.44**	9.33

Table 4-2. Fitting results of XPS (a) C 1s (Fig. 4-5) and (b) N 1s (Fig. 4-6) spectra for CN_x films deposited at 5×10^{-2} Torr (*N1*) and 1.5×10^{-1} Torr (*N2*).

	N content (at. %)	C 1s Binding Energy (eV)				
		284.3	285.4	286.3	287.4	288.8
N1	5.9	60.64	6.06	12.02	3.95	17.34
N2	6.7	55.64	6.91	5.67	2.93	28.86

	N content (at. %)	N 1s Binding Energy (eV)			
		398.3	399.2	400.1	401.6
N1	5.9	28.33	7.91	54.44	9.33
N2	6.7	8.45	6.02	57.63	27.90

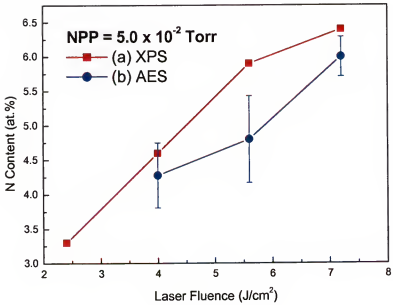

Figure 4-1. The dependence of nitrogen content on the laser fluence, observed by (a) XPS and (b) AES.

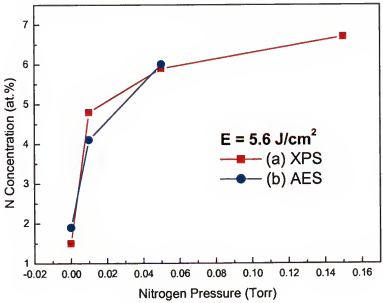

Figure 4-2. The dependence of nitrogen content on the NPP, observed by (a) XPS and (b) AES.

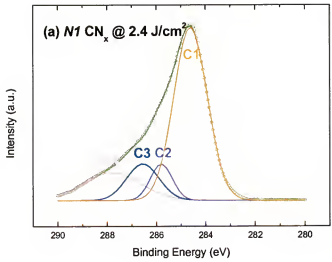

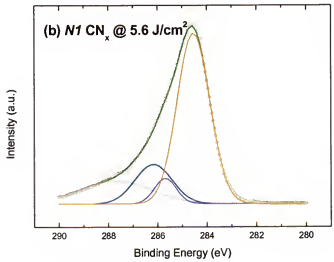

Figure 4-3. The fitted C 1s peaks of *N1* CN_x films at different energy densities.

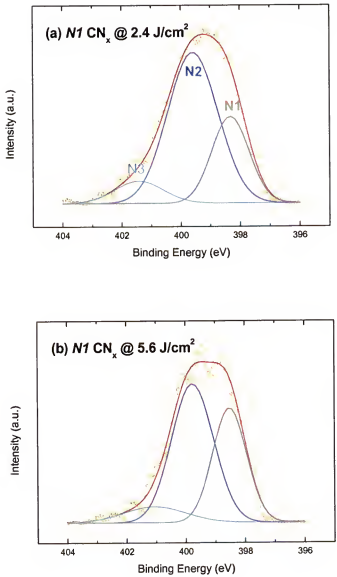

Figure 4-4. The fitted N 1s peaks of *N1* CN_x films at different energy densities.

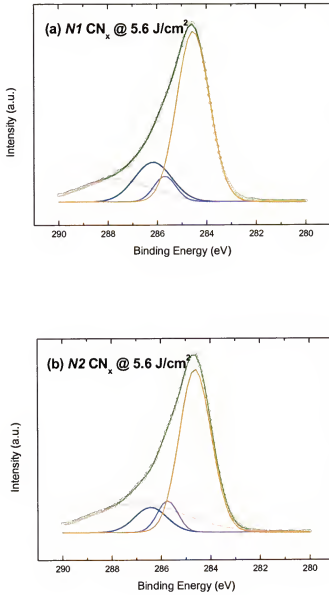

Figure 4-5. The fitted C 1s peaks of CN_x films at different NPP conditions.

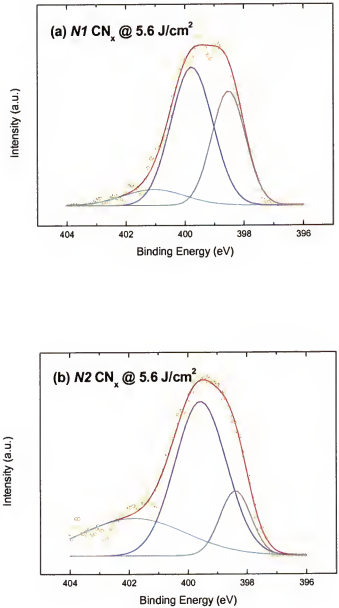

Figure 4-6. The fitted N 1s peaks of CN_x films at different NPP conditions.

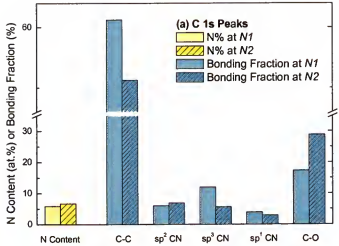

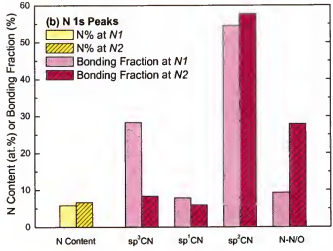

Figure 4-7. Summary of the XPS fitting results from Table 4-2.

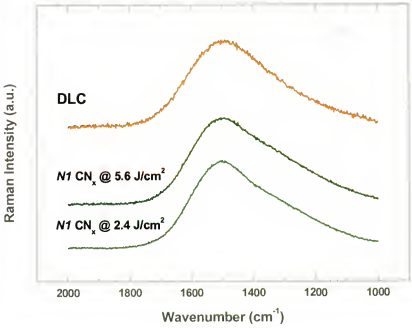

Figure 4-8. Raman spectra of CN_x films deposited at different laser fluences.

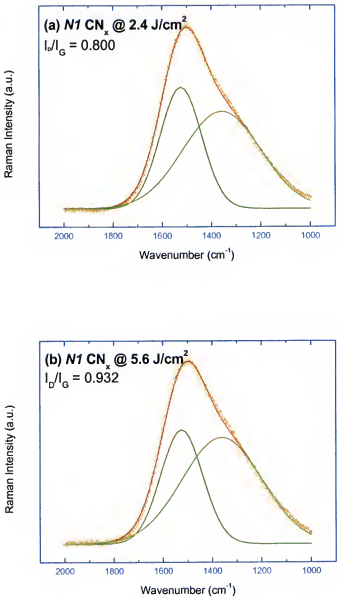

Figure 4-9. The fitted Raman spectra of CN_x films deposited at different laser fluences.

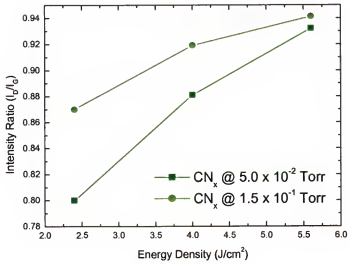

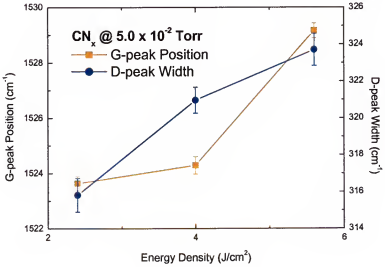

Figure 4-10. Summarized Raman results of CN_x films at different laser fluences.

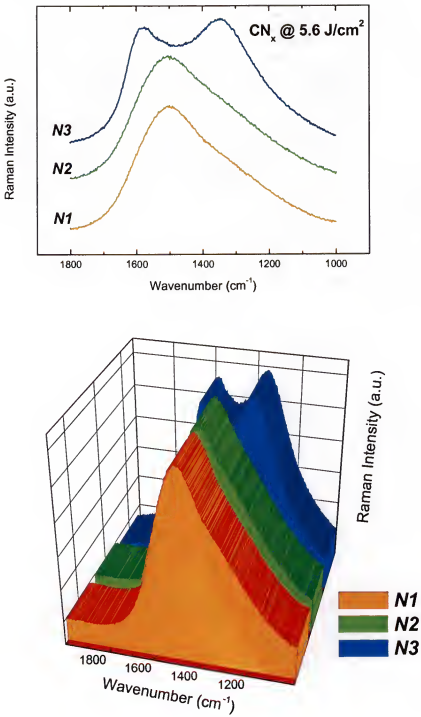

Figure 4-11. Raman spectra of CN_x films deposited at different NPP conditions.

RMS = 1.025 nm

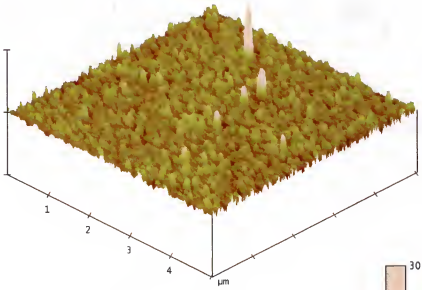

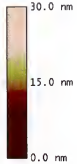

RMS = 0.627 nm

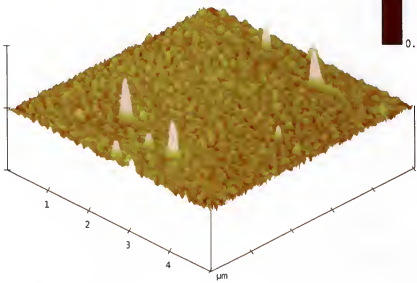

Figure 4-12. 3-D AFM images of CN_x films at *N1*: (a) 2.4 J/cm^2 and (b) 5.6 J/cm^2.

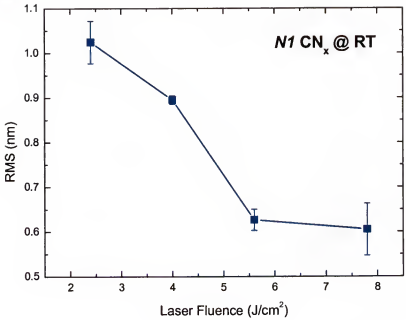

Figure 4-13. Dependence of RMS values of *N1* CN_x films on laser fluences.

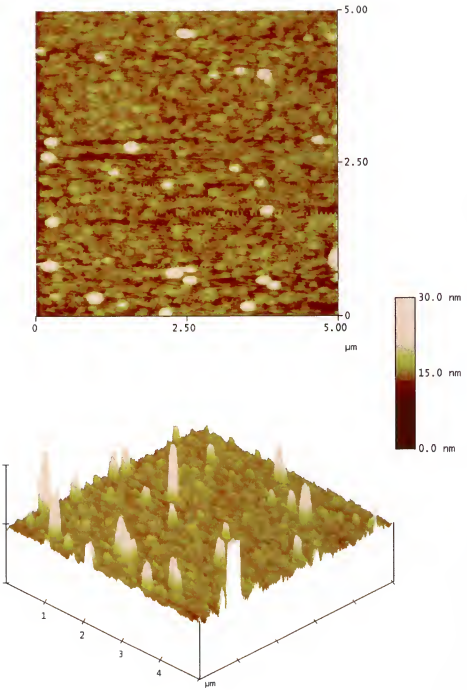

Figure 4-14. AFM images of *N2* CN_x film at 5.6 J/cm^2: RMS = 1.04 nm.

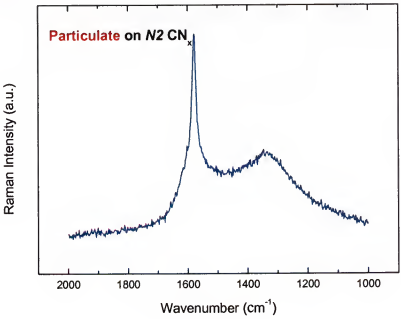

Figure 4-15. Raman spectra of the particulate on *N2* CN_x film deposited at 5.6 J/cm^2.

CHAPTER 5
INFLUENCE OF DEPOSITION TEMPERATURE ON THE MICROSTRUCTURES AND PROPERTIES OF AMORPHOUS CARBON FILMS

5.1. Effect of Substrate Temperature

The metastable structure and properties of amorphous carbon films are largely affected by the deposition parameters, such as laser energy density, process pressure, deposition rate, etc. [Gri09, Ong95, The04]. The substrate temperature is another crucial parameter deciding the film quality of amorphous carbon materials [Che02a, Rob02]. In general, the elevation of substrate temperature enhances the mobility of surface atoms, causing the evaporation of loosely bonded hydrogen atoms, the relaxation of subplanted carbon atoms, and the dissociation of weak carbon-nitrogen bonds [Che97]. These will result in the progressive graphitization and the property changes of amorphous carbon films at high temperature [Joh97, Sjo96b]..

5.2. Experimental Procedure

5.2.1. Film Synthesis

Diamond-like carbon and amorphous carbon nitride films were deposited at different temperatures. A thin layer of silver paint was applied between a sample and a thermal stage to provide the uniform heating condition. The same deposition processes, as described in earlier chapters were performed at different substrate temperatures of 100, 200, 300, and 450°C. The temperature was precisely controlled by an automated heating controller, with an increment of 10°C/minute. Prior to the deposition, a stabilization period (1 min) was allowed to remove the serration of temperature. Heating power was

cut off at the completion of deposition process. The vacuum was maintained during the cooling period. Deposited films were taken out of the chamber when the substrate temperature was read below 50°C.

5.2.2. Film Characterization

A Perkin Elmer PHI 5100 ESCA system was used to investigate the change in bonding structure of amorphous carbon films. Resolution for the multiplex analysis was 0.05 eV. Visible Raman spectra with a resolution of 1.5 cm^{-1} were obtained in the backscattering arrangement for 514 nm light from Kr ion laser (Reinshaw Rama scope-1000). The effects of substrate temperature on the morphology and RMS value of amorphous carbon surfaces were systematically observed using the AFM instrument (NanoScope® IIIa with Dimension™ 3100 Controller).

5.3. Results and Discussion

Figure 5-1 shows the variation of nitrogen contents in CN_x films depending on the substrate temperature. The films were deposited using two NPP (*N1* and *N3*) conditions at 5.6 J/cm^2. The nitrogen contents of *N1* CN_x films (Fig. 5-1 (a)) at room temperature (RT) and 300°C are 5.9% and 1.4%, respectively. Also, *N3* CN_x film deposited at 300°C shows a large drop of nitrogen content by increasing the deposition temperature (Fig. 5-1 (b)). The decrease of nitrogen content is attributed to the increase of atomic mobility at high deposition temperature. This allows the detachment of weakly-bonded volatile species, such as nitrile at high temperature. In addition, the low incorporation and high desorption rate of volatile CN(H) species at elevated temperatures also contribute to the low nitrogen contents of CN_x at high deposition temperatures [Seb98]. At 300°C, both

N1 and *N3* CN_x are almost depleted with nitrogen, showing only slightly more than 1% concentration.

Figure 5-2 shows the XPS C 1s spectra for DLC deposited at (a) RT and (b) 300°C by a laser fluence of 7.2 J/cm^2. As shown in Chapter 3, the sp^3 fraction of this film was 65% at RT. However, as the substrate temperature is raised at 300°C, the high energy shoulder at 285.2 eV is greatly reduced and results in the sp^3 fraction of only ~39%. These changes in film structures are in good agreement with the results reported in other publications, in which the thermal graphitization occurred at above 200°C [Nak04, Rob02, Voe96].

Figure 5-3 shows the XPS C 1s core level spectra of *N1* CN_x films deposited at RT and 300°C. Both films were deposited at 5.6 J/cm^2. XPS curves were fitted with the same technique used in Chapter 4. The peak at 300°C shows narrower and more symmetric shape than C 1s at RT. A relatively small tail toward the high binding energy implies there are only a few sp^{3}CN bondings existing at 300°C. The *N1* CN_x at RT shows relatively high fraction of non-aromatic CN component (15.97%) at ~ 287.2 eV. On the other hand, the aromatic component dramatically increases at 300°C. Considering the nitrogen content of CN_x at 300°C was negligible (~1.4%), this large structural change is attributed to the thermal graphitization occurred at high deposition temperature [Voe96].

Figure 5-4 shows the Raman spectra of DLC deposited at (a) RT, (b) 100, (c) 200 and (d) 300°C. All films were deposited at 7.2 J/cm^2. The G- and D-peaks at RT are also shown in the figure. It can be clearly seen that the D-peak shoulder gradually increases at high temperature. As mentioned in earlier chapters, the G-peak corresponds to the

stretching motion of sp^2 pairs in both aromatic rings and olefinic chains. On the other hand, the D-peak is associated with the breathing mode of sp^2 aromatic rings only [Fer00, Rob02]. Therefore, the increase of D-peak component shows the formation of more graphite-like structure at high temperature deposition. The detailed fitting results are demonstrated in Fig. 5-5. The I_D/I_G ratio increases from 0.61 to 1.37 at 300°C. At the same time, G-peak shows a shift toward higher wave number, implying the thermal graphitization occurred at high temperature. Also, the Raman analysis of CN_x confirms that the bonding structures of these films are more graphite-like at high temperature, as predicted with XPS results.

A precise observation on the changes of the surface morphology will provide a better understanding on the effect of the deposition temperature on the properties of amorphous carbon films. Generally, the RT deposited films exhibit very smooth surface morphologies, which inherited from their fine amorphous structures. However, a large increase of surface roughness is often observed at high temperature deposition. The contact mode AFM was used to observe the surface characteristics of amorphous carbon films deposited at different temperatures. Figure 5-6 through Fig. 5-10 show the surface morphologies and RMS values of DLC and CN_x at different deposition conditions. It can be clearly seen that the surface properties of both DLC and CN_x are greatly affected by the deposition temperature.

The 2D AMF images of DLC at 200°C and 300°C are shown in Fig. 5-6. Both films were deposited at 7.2 J/cm^2. The z-range was fixed at 30 nm to provide exact comparison. DLC at 300°C shows a coarser surface morphology with higher RMS than DLC at 200°C. The RMS values are approximately 0.237 nm and 0.340 nm for DLC at

200°C and 300°C, respectively. The RMS value was averaged from the 10 different areas of 2 μm^2. The irregularly distributed large particulates were excluded during the area selections. The increase of adatom mobility at high deposition temperature is responsible for the large RMS at 300°C. This can be related to the 'well-known' subplantation model [Lif94, McK93]. The increase of temperature results in an increase of the mobility of carbon atoms trapped in the subsurface positions of an evolving layer. As the deposition temperature increases above 200°C, these atoms become highly mobile and migrate to the surface where they follow the surface growth mode. This results in the formation of graphitic, rough films at high temperature. This was evidenced with Raman results in Fig. 5-4 and Fig. 5-5. The 3-D images provide better distinction between DLC deposited at different temperatures (Fig. 5-7). The DLC deposited at 300°C exhibits a rougher and more wrinkled surface than DLC at 200°C.

The AFM images of *N1* CN_x at 200°C and 300°C are shown in Fig. 5-8 and Fig.9. Both films were deposited at the same laser fluence of 5.6 J/cm^2. AFM scans were made on the larger area (10 $\mu m \times 10$ μm) due to the high RMS of films. Compared to *N1* CN_x at RT (Fig. 4-12 (b)), a remarkable spiky surface is observed at 200°C (Fig. 5-9 (a)), showing the RMS value at 1.212 nm. At 300°C, the film exhibits even rougher surface (RMS = 1.548 nm) with larger features compared to *N1* CN_x at 200°C. However, the shape of surface becomes more rounded at 300°C (Fig. 5-9 (b)). As predicted by XPS and Raman, the growth of large graphite grain is responsible for this morphological change of *N1* CN_x at high temperature.

Figure 5-10 shows the AFM images of *N3* CN_x deposited at 450 °C, exhibiting a very rough surface (RMS: 31.07 nm over 2 μm^2). The rainbow-colored fringes imply a large degree of thickness variation through the sample. The nanoindentation measures a extremely low hardness ($\leq$1 GPa) for this film. The elastic modulus also shows a very low value ($\leq$ 50 GPa) compared to other CN_x films (Chapter 6). These results imply the occurrence of a thermal degradation at this high temperature. There have been similar reports on the thermal degradation of CN_x films observed at $\geq$ ~400°C [Che02a, Rob02].

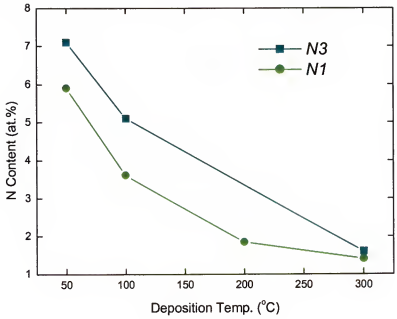

Figure 5-1. Dependence of the nitrogen contents in CN_x on the deposition temperatures.

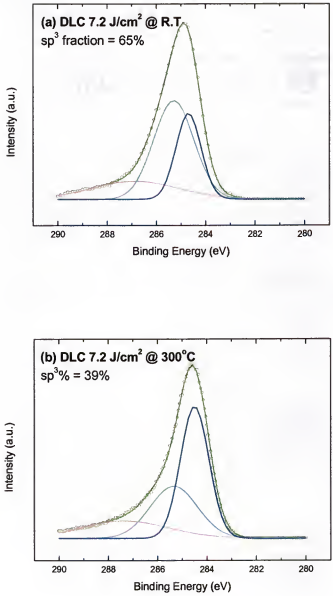

Figure 5-2. XPS C 1s spectra of DLC films deposited at different deposition temperatures.

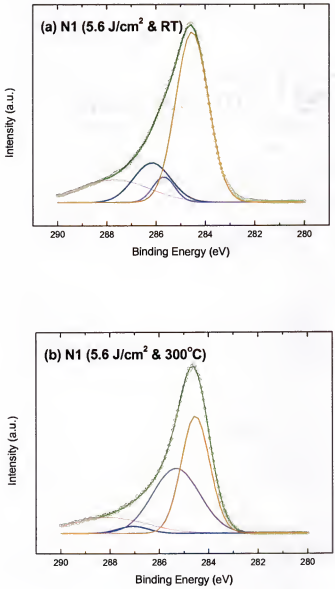

Figure 5-3. XPS C 1s spectra of *N1* CN_x films deposited at different deposition temperatures.

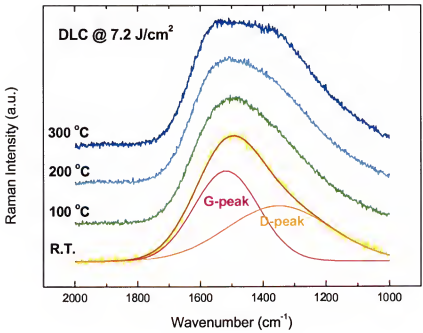

Figure 5-4. Raman spectra for DLC films deposited at different deposition temperatures.

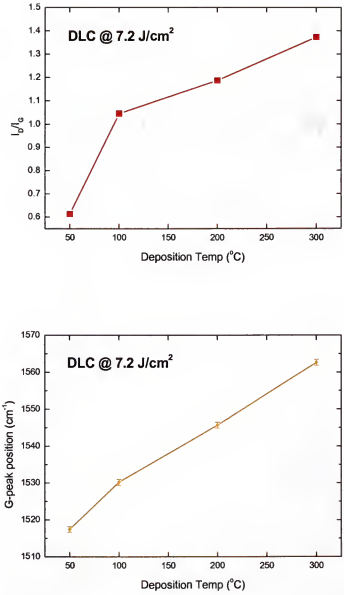

Figure 5-5. I_D/I_G ratio and G-peak position plotted as functions of deposition temperature. DLC films were deposited at a laser fluence of 7.2 J/cm^2 with a repetition rate of 5 Hz.

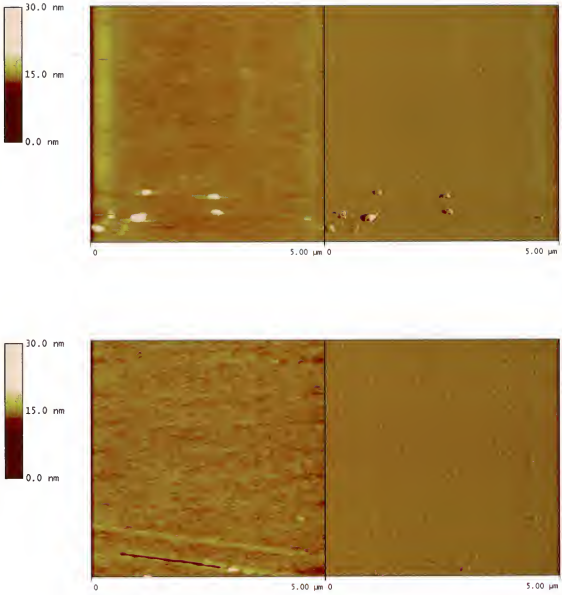

Figure 5-6. 2D AFM images of DLC films deposited at (a) 200°C and (b) 300°C.

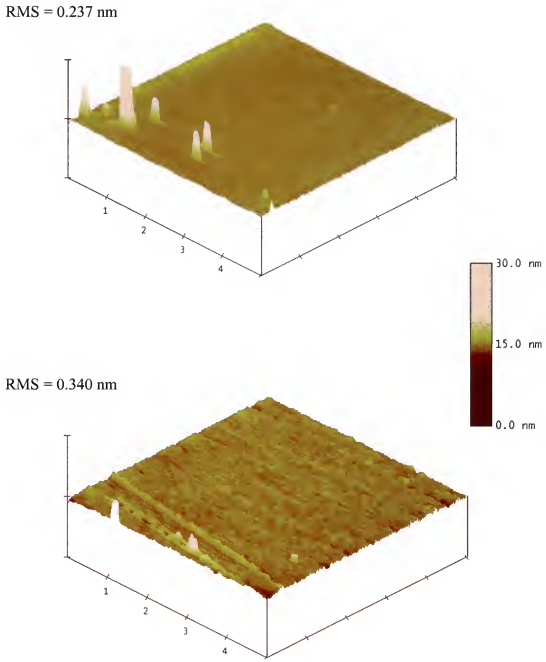

Figure 5-7. 3D AFM images of DLC films deposited at (a) 200°C and (b) 300°C.

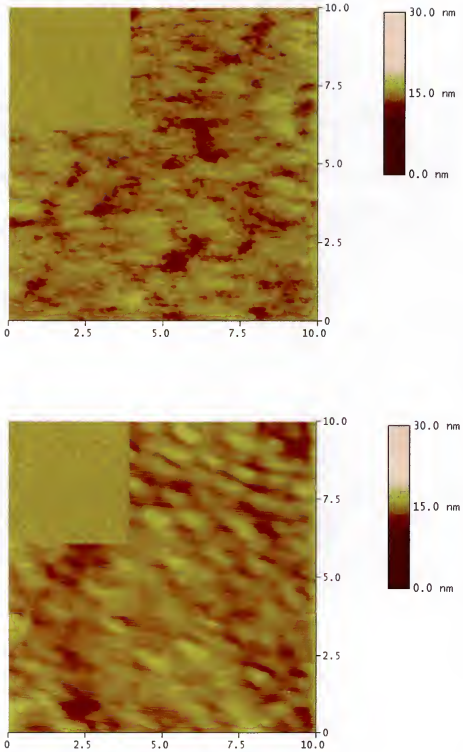

Figure 5-8. 2D AFM images of *N1* CN_x films deposited at (a) 200°C and (b) 300°C.

RMS = 1.212 nm

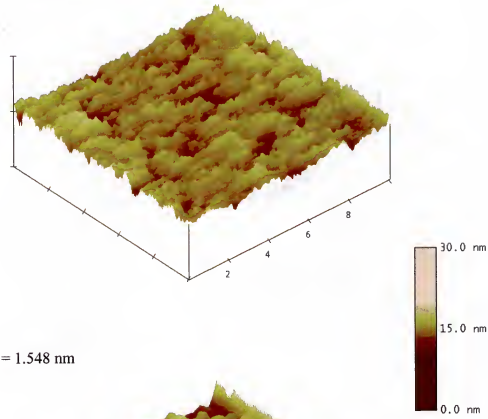

RMS = 1.548 nm

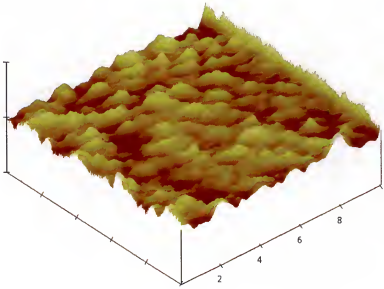

Figure 5-9. 3D AFM images of *N1* CN_x deposited at (a) 200°C and (b) 300°C.

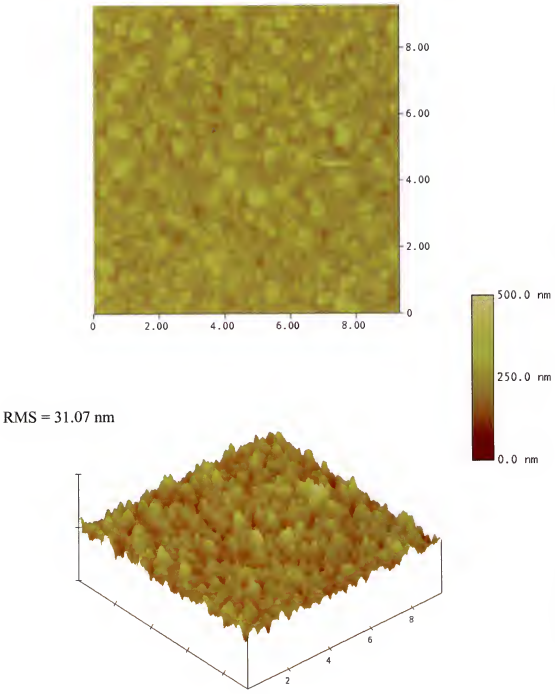

Figure 5-10. AFM images of thermally degraded *N3* CN_x deposited at 450°C.

CHAPTER 6
MECHANICAL PROPERTIES OF AMORPHOUS CARBON FILMS MEASURED BY NANOINDENTATION MEASUREMENTS

6.1. Microstructure Related Mechanical Properties

The mechanical properties of amorphous carbon materials are largely depend on their sp^3 bonding contents, the coordination defect contents, the lattice disorder, etc. [Rob01, Sul01]. The nitrogen incorporation also produces the displacement of atoms and increases the degree of disorder in the growing film [Kau92, Tam90]. All these factors are closely related to the density of amorphous carbon films. In general, the presence of coordination defects and the lattice disorder reduce the film density, while the presence of sp^3 bonds increases the diamond-like characteristic of amorphous carbon films, as well as the film density [Gue04, Rob02]. According to Robertson and Davis [Dav93, Rob93], the atomic configurations in amorphous carbon films are expected to readily adjust to the local densities produced by the highly energetic condition of ion bombardments. The local density increases if an incident ion penetrates the first atomic layer of the film and enters to an interstitial subsurface position, where it forms a bonding to its neighbor and acquires the bulk bonding of the appropriate hybridization. The formation of sp^2 hybridizations are preferred if the created density is low. On the other hand, the sp^3 hybridizations prevail at high local density. It is well known that the amorphous carbon film with a diamond-like structure (high density) exhibits the high hardness and elastic modulus values [Gri92, Rob02]. In this chapter, the nanoindentation tests are carried out to measure the nanohardness (H) and the elastic modulus (E) of amorphous carbon films.

The values of these mechanical properties will confirm the structure change of amorphous carbon films observed in previous chapters, and provide the fundamental information on deciding the feasibility of amorphous carbon coating applications.

6.2. Nanoindentation Test

The indentation measurement is a technique which evaluates the mechanical properties (H and E) of a sample to be analyzed by touching or penetrating it with another material of known properties. The nanoindentation is simply an indentation test in which the penetration depth is measured in nanometer scale, rather than microns or millimeters, which being more common in conventional hardness tests. The main goal of nanoindentation test is to extract H and E of the specimen from load-displacement measurements. The conventional indentation tests involve a measuring of the size of a residual plastic impression in the specimen as a function of indenter load. This provides the value of contact area for a given indenter load. In nanoindentation, the penetration depth beneath specimen surface is measured as the load is applied to the indenter. The known geometry of indenter then allows the contact area to be determined. This is the fundamental procedure to acquire the microhardness by nanoindentation. The nanoindentation also acquires the modulus of specimen from the contact *stiffness*, that is, the rate of change in load and depth [Fis02]. Detailed information will be provided in following sections.

6.2.1. Indentation Hardness and Modulus

The mean contact pressure is an important quantity in nanoindentation. This value is found by dividing the indenter load by the projected contact area, and is taken as the indentation hardness (H), when determined under conditions of a fully developed plastic

zone. On the other hand, the elastic modulus determined from the slope of the unloading curve is formally called the indentation or reduced modulus of the specimen material (E_r).

There is an important distinction between the conventional hardness and the hardness obtained by nanoindentation using the depth-sensing measurements. In conventional hardness tests, such as Brinell test, the size of the residual impression on the surface is used to determine the contact area and hence the hardness value. In depth sensing indentation test, such as nanoindentation, the size of the contact area under full load is determined from the depth of penetration and the shape of the elastic recovery during the removal of load. This measurement provides an estimate of the contact area under full load condition. Usually, the area given by the shape of the residual impression and that given by the depth-sensing technique are almost identical, but this is not always the case. For example, a highly elastic material, such as rubber, may give a very small residual impression while giving an appreciable contact area under load. In the former case, the hardness would be very high, while the hardness could be quite low in the latter case [Fis02].

6.2.2. Load-Depth Compliance Curves

The principal goal of nanoindentation is to extract the hardness and the elastic modulus of specimen from the measurements of indenter load and penetration depth. In general, the load and depth of penetration are recorded as load is applied from zero to some maximum and then from the maximum load back to zero. If plastic deformation occurs, then there is a residual impression left on the surface of the specimen. Unlike the conventional indentation tests, the size of residual impression for nanoindentation is too small to measure accurately with optical techniques. Instead, the depth of penetration, together with the known geometry of the indenter provides an indirect measure of the

contact area at full load, from which the mean contact pressure, thus hardness, is estimated. On the removal of load, the material attempts to regain its original shape, but this is limited by plastic deformation occurred during loading procedure. However, there is some degree of recovery due to the relaxation of elastic strains within the material. An analysis of the initial portion of this elastic unloading response gives an estimate of the elastic modulus of the indented material [Fis02].

The equations used to acquire the hardness (H) and Young's modulus (E) are described as follows:

$$H = \frac{P_{\max}}{A} = c_b \sigma_y \tag{6.1}$$

$$S = \frac{dP}{dh} = \beta \frac{2}{\sqrt{\pi}} \sqrt{A} E_r \tag{6.2}$$

where σ_y is the yield stress, c_b is the constraint factor depending on the indenter shape and the material properties, P is the indentation load, $P_{\max}$ is the maximum indentation load, S is the contact stiffness, h is the displacement, A is the projected contact area, E_r is the reduced modulus, and β is the geometric or correction factor that depends on the indenter shape. The value of constant β is 1.000 for the circular shape, 1.034 for the triangular shape, and 1.012 for the square shape of indenter.

On the other hand, E_r is defined as follows:

$$E_r = \frac{\left(1-\nu^2\right)}{E} + \frac{\left(1-\nu_i^2\right)}{E_i} \tag{6.3}$$

where E and ν are the young's modulus and the Poisson's ratio of substrate, and E_i and ν_i are the properties of a diamond indenter, respectively. Because Young's modulus of diamond (E = 1140 GPa) is usually larger than that of the sample by one or two orders of

magnitude, the reduced modulus can effectively represent the Young's modulus of the sample. $S = dp/dh$ is the experimentally measured contact stiffness of the upper portion of the unloading curve. Figure 6-1 shows the load-displacement curves for PLD deposited DLC films at different energy densities. Unloading curve with a stiffer slope results in higher H and E_r [Fis02, Sei96] For the accurate measurement, the indentation depth must be limited to a fraction of order 10% of the total film thickness [Fis02, Pha92, Rob02]. This is particularly important for the case of hard on soft films, such as DLC [Hos89].

6.3. Results and Discussion

Nanoindentation measurements were performed using the Triboindenter® with Triboscope® manufactured by Hysitron. Figure 6-2 shows the experimental setup for nanoindentation [*www.hysitron.com*]. It has been reported that the mechanical properties of amorphous carbon films are tailored by the relative amount of sp^2 and sp^3 bondings in their structure [Hos89, Rob91, Sav92, Wei99]. In general, the high hardness and modulus are related with the increasing sp^3/sp^2 bonding ratio in their structure. On the other hand, the development of sp^2 aromatic bonding or the presence of nitrogen in amorphous carbon structure results in the reduction of mechanical properties.

An amorphous quartz substrate (E_r = 69.6 GPa and H = 9.3 GPa) was used to confirm the calibrated area function of indenter, which is required to provide the quantitative data of hardness and Young's modulus from load-displacement curves. The mechanical properties of the amorphous quartz started to decrease below the contact depth of ~5 nm. It happened due to the truncation of the diamond tip indent [Saw99]. Therefore, the experimental results obtained below the contact depth of ~5 nm were neglected. Also, some erroneous results were excluded from the each measurement.

Figure 6-3 shows the hardness and the reduced modulus of DLC films deposited at 4.0 J/cm^2 and 7.2 J/cm^2. The result of bare Si substrate is also included in the figure. The indentations were performed according to the displacement-time sequence in Fig. 6-4. The indenter was loaded to a certain indentation depth during the first 10 sec, dwelled for 5 sec, and then unloaded for the next 10 seconds. The dwell period allows any time-dependent plastic effects (e.g. creep) to diminish.

The Si substrate exhibits relatively low H and E_r values of 6.88 GPa and 124.51 GPa, respectively. On the other hand, DLC coatings show the dramatically enhanced mechanical properties. DLC deposited at 4.0 J/cm^2 shows H of 15.86 GPa, which is more than twice as high as that of Si substrate. DLC coating produced at higher laser fluence (7.2 J/cm^2) exhibited even higher H (21.42 GPa), which considered as the result of higher degree of sp^3 network in DLC at 7.2 J/cm^2 (65% sp^3) than DLC at 4.0 J/cm^2 (24% sp^3) (Fig. 3-13). As mentioned earlier, the hardness and elastic modulus of amorphous carbons, including DLC follow the variation of sp^3 fraction quite closely [Rob91, Wei99]. The H and E of amorphous carbons depend on the degree of sp^3 carbon network and the average coordination of the network. In addition, the elastic modulus is also largely affected by the rigidity of the individual bonds [Rob02, Wei99]. The effect of rigidity and coordination can be explained by the constraint-counting model [He85, Phi79]. For a network with low coordination, there are many ways to deform the network easily. A network must be constrained in order to be rigid and hard [Rob92]. A little modification is required for considering the effect of graphitic clusters. Although a graphite layer is three-fold coordinated, the sp^2 aromatic phase constraints mostly within the two dimensions of layer and contribute little in three dimensional networks [Rob92].

Generally, the sp^3 bondings affect the mechanical properties while the sp^2 sites control the electronic properties of amorphous carbon materials [Rob86, Rob92].

Figure 6-5 shows the *in-situ* images of indentation process performed on a DLC film surface. The maximum load was ~2000 μN at the indentation depth of ~70 nm. The trace of indentation becomes more apparent as the indentation depth increases. In each measurement, the sample was indented 50 times by the automated displacement control mode. To avoid the substrate effect, the maximum indentation depths were selected between 40 and 70 nm depending on the thickness of each sample. Figure 6-6 compares the mechanical properties (H & E_r) of DLC at four different laser energy densities. Again, H and E_r of amorphous carbon films are closely related with the sp^3 fraction in their structure, and increase monotonically as the sp^3 fraction of film increased at high laser fluence. Figure 6-7 shows a clear vision of enhanced mechanical properties of DLC films at high laser density. However, the decrease of mechanical properties at very high energy has been reported by other researchers [Jia89, Koi90, Rob02]. The softening was explained by the formation of more graphitic bondings due to the thermalization and relaxation by extremely energetic ions at very high voltages.

As observed in Chapter3, DLC produced by the multi-cycle process did not show any sign of film delamination. This was explained by the formation of a sp^2-rich intermediate layer at the end of each cycle. Nevertheless the formation of this low density layer, the multi-cycle deposited DLC films show relatively high values of H and E_r, which comparable to those reported elsewhere [Rob02, Wei99]. On the other hand, DLC deposited by the single-cycle process at 6.4 J/cm^2 shows slightly higher H and E_r (23.47 GPa and 229.71 GPa, respectively) than DLC by the multi-cycle process at 7.2 J/cm^2.

However, as already seen, this film suffered buckling process due to high internal stress, which made this film unable to use as protective coating material. On the other hand, by controlling the laser fluence, the multi-cycle process can produce high quality DLC coatings with various mechanical properties for specific applications.

The nanoindentation measurements were also performed on CN_x films. The results are shown in Fig. 6-8 and Fig. 6-9. When compared to DLC deposited at the same laser fluence, each CN_x film shows lower H and E_r values. The H of CN_x at 5.6 J/cm^2 is ~35% lower than that of DLC deposited at same laser fluence. The E_r of CN_x also shows ~25% lower value. The enhanced formation of sp^2 aromatic phase due to the incorporation of nitrogen and the high process pressure are responsible for this reduction. However, like DLC, the nanoindentation measurements reveal that the mechanical properties of CN_x films also can be controlled by laser fluence, and H and E_r of CN_x at high laser fluence are large enough for the application in magnetic heads and hard disks [Bhu99, Gog01].

The effect of the deposition temperature on the structure change in amorphous carbon films also can be observed by nanoindentation test. Evaluation of the mechanical properties at high temperature is an important task to check the validity of amorphous carbon coatings at different temperature range. By knowing the high temperature behavior, for example the thermal degradation, the possible catastrophic coating failure can be prevented in a high temperature environment. Figure 6-10 shows H and E_r of DLC films deposited at different temperatures as functions of contact depth. Both H and E_r drop largely at high deposition temperature. Compared to DLC deposited at RT, the film at 300 °C exhibits H of only a half magnitude (21.42 GPa *vs.* 11.03 GPa). The E_r also shows a large drop at high temperature. These changes can be evidenced by the fact that

more graphite-like structures were developed in DLC deposited at higher temperatures, as discussed in chapter 5. Figure 6-11 shows the decreasing trend of H and E_r at high deposition temperatures. Although both values are decreased in a large degree, there was no sign of DLC thermal degradation up to 450°C. Similar trend was also observed from the CN_x films deposited at high temperatures. The mechanical properties of CN_x become softer at higher temperatures. However, *N3* CN_x showed thermally degraded behavior at 450 °C. This film showed very rough morphology with large features in Fig. 5-10. The z-range used for measuring this sample was 500 nm, resulting in the RMS of 31.07 nm. The erroneous behaviors of the load-displacement curve were probably affected by this huge roughness and non-uniformity (Fig. 6-12). Surface roughness is very important in the nanoindentation measurement. Since the contact area is measured indirectly from the penetration depth, the natural roughness of the real surface can cause errors in determining the contact area between the indenter and the specimen [Fis02, Gre71]. The overall effect of surface roughness is reported to reduce the mean contact pressure by increasing the contact radius. Thus, for a given indenter load, the depth of penetration is reduced and the computed E_r is also reduced [Fis02].

Figure 6-13 shows the hardness and reduced modulus values measured from load-displacement curves shown in Fig. 6-12. The H results show scattered values ranging between 0.14 and 0.96 GPa. The E_r measurements also exhibit abnormally low values of less than 50 GPa. Together with the very high RMS on a non-uniform surface, these low H and E_r imply the occurrence thermal degradation at this temperature. Therefore, the use of CN_x film should be kept below 450°C to avoid the coating failure during the high temperature applications.

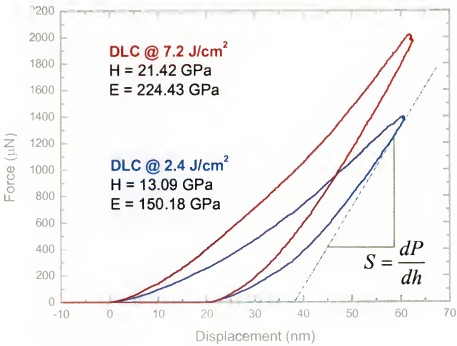

Figure 6-1. The load-displacement curves for PLD deposited DLC films deposited at different energy densities.

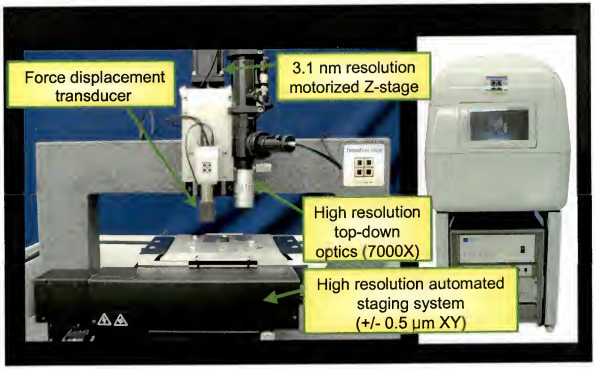

Figure 6-2. Schematic demonstration of Triboindenter® with Triboscope® by Hysitron.

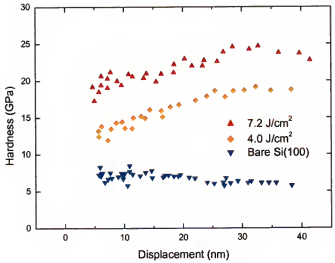

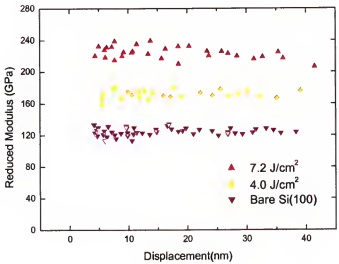

Figure 6-3. The H and E_r of multi-cycle deposited DLC films on Si (100) substrates.

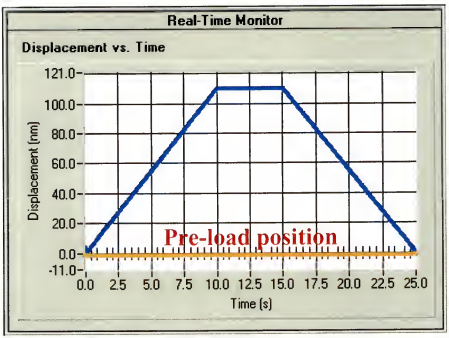

Figure 6-4. The displacement and time sequence used for the nanoindentation.

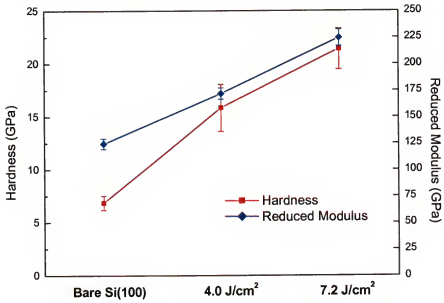

Figure 6-5. Comparison of H and E_r for bare Si (100) and DLC coatings.

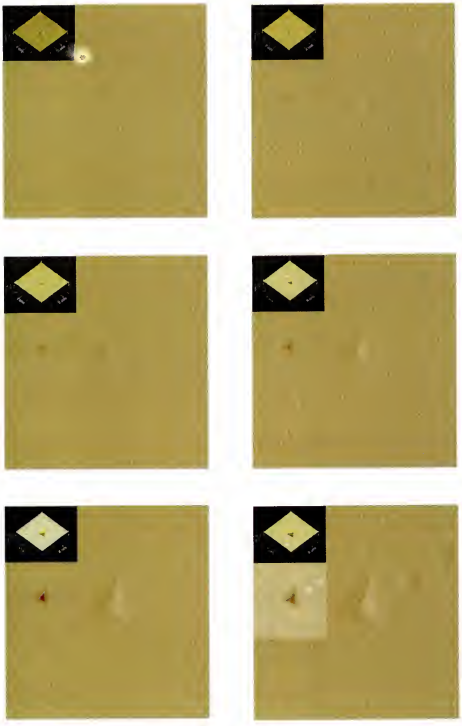

Figure 6-6. *In-situ* images of nanoindentation process performed on a DLC film.

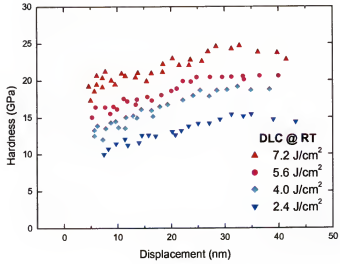

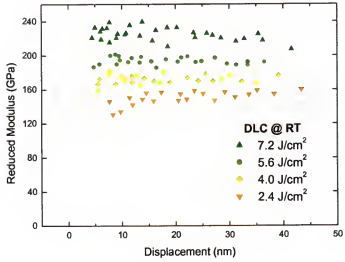

Figure 6-7. The H and E_r values of DLC films deposited at different laser fluences.

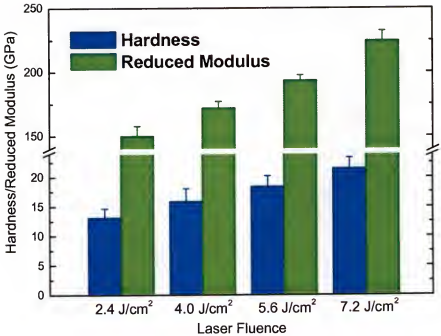

Figure 6-8. The change in mechanical properties of DLC by different laser fluences.

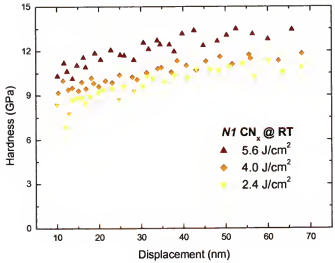

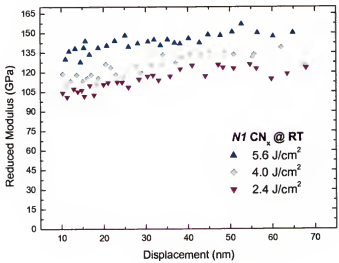

Figure 6-9. The H and E_r values of CN_x films deposited at different laser energy densities.

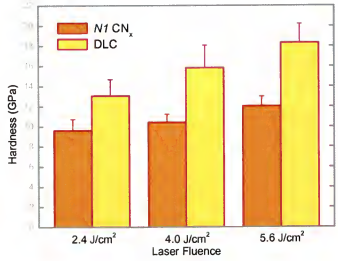

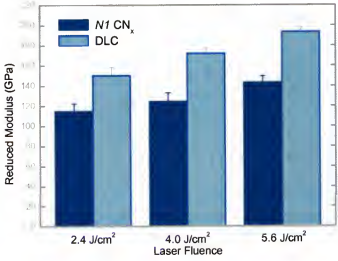

Figure 6-10. Comparison of H and E_r between DLC and $N1$ CN_x at different laser fluences.

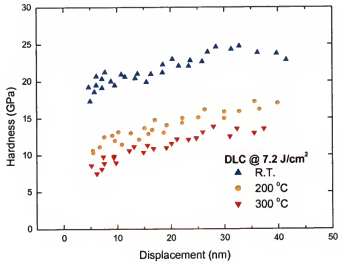

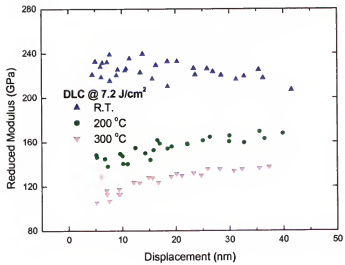

Figure 6-11. The H and E_r of DLC films deposited at different substrate temperatures.

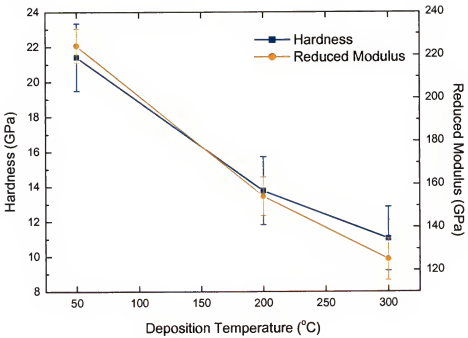

Figure 6-12. Dependence of H and E_r of DLC on the deposition temperature.

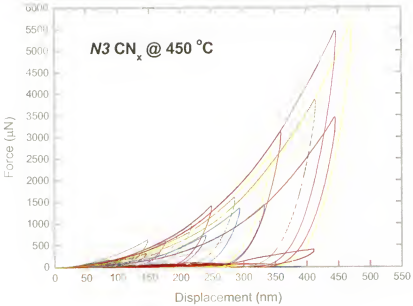

Figure 6-13. Load-displacement curve of *N3* CN_x deposited at 450°C.

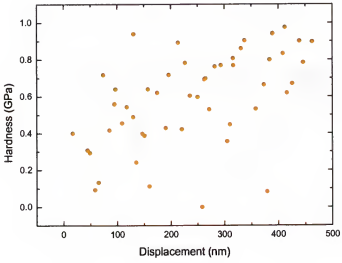

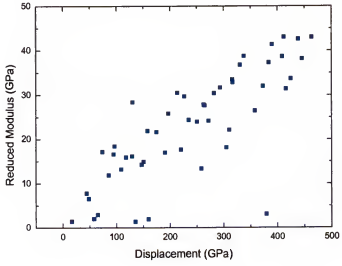

Figure 6-14. Mechanical properties of thermally degraded *N3* CN_x at 450°C.

CHAPTER 7
CONCLUSION

A multi-cycle process was used to produce high quality DLC with low residual stress. DLC films were prepared at high vacuum condition (< ~10^{-6} Torr). The DLC structures were characterized by Raman, XPS, and AFM. A surface profilometer was used to determine the parameters needed for the stress measurements, including the films thickness. Raman results revealed that I_D/I_G decreased from 1.16 to 0.61 as the laser fluence increased from 2.4 J/cm^2 to 7.2 J/cm^2. This was explained by the formation of DLC with high sp^3 content at high laser energy. The enhanced sp^3 fraction was evidenced by XPS, and the sp^3 bonding fraction increased from 16% to 65% in the above energy density range. DLC deposited by a single-cycle process exhibited slightly higher sp^3 content compared to DLC produced by the multi-cycle process. However, the single-cycle deposited DLC suffered coating failure due to high intrinsic stress ($\geq$ 5.6 GPa) developed during the coating condensation. On the other hand, AFM measurements revealed that DLC by the multi-cycle deposition exhibited relatively smooth surface morphologies without any sign of delamination, which attributed to the low residual stress (~3 GPa). Stress-releasing mechanism of the multi-cycle process was explained by the interruption of over-constrained structure with the low density intermediate layer formed at the end of each cycle. In addition, the nanoindentation measurements showed DLC produced by the multi-cycle process exhibited the similar values of hardness and elastic modulus compared to the single-cycle deposited DLC. Therefore, the multi-cycle

process has been proved to be an effective deposition method to produce high-quality DLC coatings without stress-induced delamination.

Amorphous carbon nitride (CN_x) films were also studied as another low stress coating material. Films were formed using 3 different NPPs (*N1*: 5×10^{-2} Torr, *N2*: 1×10^{-1} Torr, & *N3* = 5×10^{-1} Torr) at 4 different laser energy densities (2.4 J/cm^2, 4.0 J/cm^2, 5.6 J/cm^2, & 7.2 J/cm^2). Nitrogen was more effectively incorporated into CN_x deposited at high NPP and/or high laser density. XPS results showed that the high laser fluence stimulated the formation of diamond-like sp^3CN bondings in CN_x films. On the other hand, the CN_x deposited at high NPP showed a decreased amount of sp^3CN bondings with increased nitrogen content. However, it has been revealed that a large portion of this incorporated nitrogen exist without bonding to the carbon network. The I_D/I_G of CN_x increased at high laser fluences. This was explained by the effect of increased nitrogen content at high laser fluence. AFM measurements revealed that CN_x with more sp^2 component showed a rougher surface than DLC. However, the CN_x films generally exhibit slightly lower stress values (1.78–3.01 GPa).

The changes in the bonding structures of amorphous carbon films at $\leq$ 450°C were investigated by XPS and Raman spectroscopy. The nitrogen content in CN_x continuously decreased at high temperature deposition. This was ascribed to the enhanced atomic mobility at high temperature, which led to the loss of volatile CN species. The XPS results revealed that the sp^3 content was greatly reduced in 300°C deposited DLC, implying the enhanced formation of graphite-like structure at high temperature. The thermal graphitization was also observed in high temperature deposition of CN_x films. The changes in surface morphologies were closely observed by contact mode AFM. In

general, the amorphous carbon films deposited at high temperature exhibited rougher surfaces, showing the formation of graphite-rich films. The *N3* CN_x at 450°C exhibited very rough morphology, implying the occurrence of a thermal degradation.

Finally, the nanoindentation tests were carried out to measure the nano-hardness and the elastic modulus of amorphous carbon films. These mechanical properties confirmed the structure change of amorphous carbon films observed in the previous chapters, and provided the fundamental information on deciding the feasibility of various coating applications. Amorphous carbon film with high sp^3 content is known to show superior mechanical properties. However, the strong film characteristic usually accompanies high internal stress developed during the coating condensation process. Therefore, it is very important to optimize the deposition conditions at which the high quality amorphous carbon coating can be produced without delamination. In earlier chapters, various amorphous carbon films were formed by PLD process. The multi-cycle deposited DLC and the single-cycle deposited CN_x showed effectively lowered residual stress values and there was no sign of coating failure. On the other hand, the nano-indentation revealed that the mechanical properties of these non-delaminated films were effectively controlled by the process parameters, and the values of H and E_r were high enough for the application in magnetic heads and hard disks. The *N3* CN_x deposited at 450°C showed extremely low H and E_r values, confirming the occurrence of thermal degradation. However, no significant softening was observed from DLC at 450°C.

LIST OF REFERENCES

[Ais71] S. Aisenberg and R. Chabot, J. Appl. Phys. **42**, 2953 (1971).

[Alv98] F. Alvarez and N. M. Victoria, Appl. Phys. Lett. **73(8)**, 1065 (1998).

[And97] S. Anders, D. L. Callahan, G. M. Pharr, and C. S. Bhatia, Surf. Coatings Technol. **94**, 189 (1997).

[Ant97] A. Antilla, R. Lappalainen, V. M. Tiainen, and M. Hakovirta, Adv. Mater. **9**, 1161 (1997).

[Ban99] F. Banhart, Rep. Prog. Phys. **62**, 1181 (1999).

[Bhu99] B. Bhushan, Diam. Relat. Mater. **8**, 1985 (1999).

[Bro98] I. G. Brown, Ann. Rev. Mater. Sci. **28**, 243 (1998).

[Che97] L. C. Chen, D. M. Bhrsari, C. Y. Yang, K. H. Chen, T. J. Chuang, and M. C. Lin, Thin Solid Films **303**, 66 (1997).

[Che99] Y. H. Cheng, Y. P. Wu, J. G. Chen, and C. Xie, Diam. Relat. Mater. **7(8)**, 1214 (1999).

[Che00] Y. H. Cheng, B. K. Tay, S. P. Lau, X. L. Qiao, and C. S. Xie, Diam. Relat. Mater. **9**, 2010 (2000).

[Che01] X. Chen, and J. J. Vlassak, J. Mater. Res. **16**, 2974 (2001).

[Che02a] Y. H. Cheng, X. L. Qiao, J. G. Chen, Y. P. Wu, C. S. Xie, Y. Q. Wang, D. S. Xu, S. B. Mo, and Y. B. Sun, Diam. Relat. Mater. **11**, 1511 (2002).

[Che02b] Y. H. Cheng, X. L. Qiao, J. G. Chen, Y. P. Wu, C. S. Xie, Y. Q. Wang, D. S. Xu, S. B. Mo, and Y. B. Sun, Surf. Coat. Technol. **160**, 269 (2002).

[Che94] J. T. Cheng, *Pulsed Laser Deposition of Thin Films*, John Wiley & Sons, New York (1994).

[Chh97] M. Chhowalla, J. Robertson, C. W. Chen, S. R. P. Silva, and G. A. J. Amaratunga, J. Appl. Phys. **81**, 139 (1997).

[Cho90] N. H. Cho, K. M. Krishnan, D. K. Vries, M. D. Rubin, C. B. Hopper, B. Brushan, and D. B. Bogy, J. Mater. Res. **5**, 2543 (1990).

[Cue94] A. Cuesta, P. Damelincourt, J. Laureyns, A. Martinez-Alonso, and J. M. D. Tascon, Carbon **32**, 1523 (1994).

[Cuo91] J. J. Cuomo, J. P. Doyle, and J. C. Liu, Appl. Phys. Lett. **58**, 466 (1991).

[Dav93] C. A. Davis, Thin Solid Films **226**, 30 (1993).

[Dav98] C. A. Davis and K. M. Knowles, Phys. Rev. Lett, **80**, 3280 (1998).

[Dec97] T. Decker, G. P. Lundie, D. L. Pappas, R. P. Welty, and R. C. Parent, *US Patent* No. 5,992,268: Amorphous diamond coating of blades (1997).

[Dim91] H. Dimigen, Surf. Coat. Technol. **49**, 453 (1991).

[Dre82] G. Dresselhaus, and R. Al-Jishi, Phys. Rev. B **26**, 4514 (1982).

[Dre96] M. S. Dresselhaus, G. Dresselhaus, and P. C. Eklund, *Science of Fullerenes and Carbon Nanotubes*, Academic Press, London (1996).

[Erd01] A. Erdemir, C. Donnet, *Tribology of Diamond, Diamond-Like Carbon and Related Films, Modern Tribology Handbook*, CRC Press, Warwick 888 (2001).

[Fal93] P. J. Fallon and L. M. Brown, Diam. Relat. Mater. **2**, 1004 (1993).

[Fer00] A. C. Ferrari, and J. Robertson, Phys. Rev. B. **61**, 14095 (2000).

[Fie79] J. Field, *The Properties of Diamond*, Academic Press, New York & London (1979).

[Fis02] A. C. Fischer-Cripps, *Nanoindentation*, a Mechanical Engineering Series, Springer, New York (2002).

[Fra92] D. F. Franceschini and C. A. Achete, Appl. Phys. Lett. **60**, 3229 (1992).

[Gan25] A. Gangopadhyay, Tribol. Lett. **5**, 25 (1998).

[Gas91] P. H. Gaskell, Phys. Rev. Lett. **67**, 1286 (1291).

[Gor94] A. A. Goruppa, Diam. Relat. Mater, **3**, 1223 (1994).

[Gre71] J. A. Greenwood, and J. H. Tripp, Proc. Inst. Mech. Eng. **185**, 625 (1971).

[Gri92] A. Grill, and V. Patel, Appl. Phys. Lett. **60**, 2089 (1992).

[Gri93] M. Grischke and K. Bewilogua, Mater. Manuf. Process. **8**, 407 (1993).

[Gri99] A. Grill, Diamond Relat. Mater. **8**, 428 (1999).

[Gog01] P. Goglia, J. Berkowitz, J. Hoehn, A. Xidis, and L. Stover, Diam. Relat. Mater. **10**, 271 (2001).

[Gor89] A. A. Gorbunov and V. I. Konov, Phys. Tech. Lett. **34**, 77 (1989).

[Gue04] M. Guerino, M. Massi, H. S. Maciel, C. Otani, R. D. Mansano, P. Verdonck, and J. Libardi, Diam. Relat. Mater. **13**, 316 (2004).

[Hae02] R. Haerle, E. Riedo, and A. Baldereschi, Phys. Rev. B **65**, 45101 (2002).

[Hay00] T. Hayashi, A. Matsumuro, M. Muramatsu, M. Kohzaki, and K. Yamaguchi, Thin Solid Films **376**, 152 (2000).

[He85] H. He, and M. F. Thorpe, Phys. Rev. Lett. **54**, 2107 (1985).

[Hel99] N. Hellgren, M. P. Johansson, E. Broitman, L. Hultman, and J. E. Sundgren, Phys. Rev. B **59(7)**, 5162 (1999).

[Hof98] H. Hofsass, H. Feldermann, R. Merk, M. Sebastian, and C. Ronning, Appl. Phys. **A66**, 153 (1998).

[Hos89] S. Hoshino, K. Fujii, N. Shohata, H. Yamaguchi, Y. Tsukamoto, and M. Yanagisawa, J. Appl. Phys. **65**, 1918 (1989).

[Jac93] W. Jacob, and W. Moller, Appl. Phys. Lett. **63**, 1771 (1993).

[Jam97] C. Jama, V. Rousseau, O. Dessaux, and P. Goudmand, Thin Solid Films **302**, 58 (1997).

[Jia89] X. Jiang, J. W. Zou, and P. Grunberg, J. Appl. Phys. **66**, 4729 (1989).

[Jia90] X. Jiang, K. Reichelt, and B. Stritzker, J. Appl. Phys. **66**, 5805 (1990).

[Joh97] D. J. Johnson, Y. Chen, and Y. He, Diam. Relat. Mater. **6**, 1799 (1997).

[Kau89] J. N. Kaufman and D. D. Superstein, Phys. Rev. B **18**, 13053 (1989).

[Kau92] H. P. Kaukonen, and R. M. Nieminem, Phys. Rev. Lett. **68**, 620 (1992).

[Koh95] T. Kohler and T. Frauenheim, Phys. Rev. B **52**, 11837 (1995).

[Koi90] P. Koidl and C. Wagner, Mater. Sci. Forum **52**, 41 (1990).

[Koi92] J. Koike and D. M. Parkin, Appl. Phys. Lett. 60, 1450 (1992).

[Koi99] K. J. Koivusaari and J. Levoska, J. Appl. Phys. **85(5)**, 2915 (1999).

[Kro85] H. Kroto, J. Heath, and S. O'Brian, Nature **318**, 162 (1985).

[Lee97] D. H. Lee, H. Lee, and B. Park, Appl. Phys. Lett. **23(70)**, 3104 (1997).

[Lif90] Y. Lifshitz, S. R. Kasi, and W. Eckstein, Phys. Rev. B **41**, 10468 (1990).

[Lif94] Y. Lifshitz and G. D. Lempert, Phys. Rev. Lett. **72(17)**, 2753 (1994).

[Lif95] Y. Lifshitz and E. Grossman, Diam. Relat. Mater. **4**, 318 (1995).

[Liu89] A. Y. Liu, and M. L. Cohen, Science **245**, 841 (1989).

[Liu90] A. Y. Liu, and M. L. Cohen, Phys. Rev. B **41**, 10727 (1990).

[Lop96] G. P. Lopinski, and J. S. Lannin, Appl. Phys. Lett. **69**, 3348 (1996).

[Low98] D. H. Lowndes, Exp. Methods. Phys. Sci. **30**, 475 (1998).

[Mat94] A. Matthews, and S. S. Eskildsen, Diam. Relat. Mater. **3**, 902 (1994).

[McK91] D. R. McKenzie and D. Muller, Phys. Rev. Lett. **67**, 773 (1991).

[McK93] D. R. McKenzie, J. Vac. Sci. Technol. B **11**, 1928 (1993).

[McK96] D. R. McKenzie, Rep. Prog. Phys. **59**, 1611 (1996).

[Mem86] R. Memming and H. J. Tolle, Thin Solid Films **143**, 31 (1986).

[Mer97] P. Merel and M. Chaker, Appl. Phys. Lett. **71(26)**, 3814 (1997).

[Mer98] P. Merel, M. Tabbal, and M. Chaker, Appl. Surf. Sci. **136**, 105 (1998).

[Miz87] Y. Mizokawa, T. Miyasato, S. Nakamura, and C. W. Wilmsen, J. Vac. Sci. Technol. A **5**, 2809 (1987).

[Mol91] W. Moller, Appl. Phys. Lett. **59**, 2391 (1991).

[Muh99] S. Muhl, and J. M. Mendez, Diam. Relat. Mater. **8**, 1809 (1999).

[Nak04] H. Nakazawa, Y. Yamagata, M. Suemitsu, and M. Mashita, Thin Solid Films **467**, 98 (2004).

[Ner79] R. J. Nermanich and S. A. Solin, Phys. Rev. B **20**, 392 (1979).

[Niu93] C. Niu, Y. Z. Lu, and C. M. Lieber, Science **261**, 334 (1993).

[Ogu91] K. Oguri, and T. Arai, Surf. Coatings Technol. **47**, 710 (1991).

[Ong95] C. W. Ong, X. A. Zhao, J. T. Cheung, S. K. Lam, Y. Liu, C. L. Choy, and P. W. Chan, Thin Solid Films **258**, 34 (1995).

[Pan95] O. S. Panar, D. Sarangi, S. Kumar, P. Dixit, and R. Bhattacharyya, J. Vac. Technol. A **13**, 2519 (1995).

[Pap94] D. L. Pappas, and J. Hopwood, J. Vac. Sci. Technol. A **12**, 1576 (1994).

[Par02] C. K. Park, S. M. Chang, H. S. Uhm, S. H. Seo, and J. S. Park, Thin Solid Films **420-421**, 235 (2002).

[Pha92] G. Pharr, W. C. Oliver, Mater. Res. Soc. Bull. **17**, 28 (1992).

[Phi79] J. C. Philis, J. Non Cryst. Solids **34**, 153 (1979).

[Pie93] H. O. Pierson, *Handbook of Carbon, Graphite, Diamond and Fullerenes*, Noyes Publications, New Jersey (1993).

[Pra96] S. Prawer, K. W. Nugent, Y. Lifshitz, G. D. Lempert, E. Grossman, J. Kulik, I. Avigal, and R. Kalish, Diam. Relat. Mater. **5**, 433 (1996).

[Rie00] E. Riedo, F. Comin, and J. Chevrier, J. Appl. Phys. **88**, 4365 (2000).

[Ris98] J. Ristein, R. T. Stief, and W. Beyer, J. Appl. Phys. **84**, 3836 (1998).

[Rob86] J. Robertson, Surf. Coat. Technol. **50**, 317 (1986).

[Rob91] J. Robertson, Prog. Solid State Chem. **21**, 199 (1991).

[Rob92] J. Robertson, Phys. Rev. Lett. **68**, 220 (1992).

[Rob93] J. Robertson, Diam. Relat. Mater. **2**, 984 (1993).

[Rob94] J. Robertson, Pure Appl. Chem. **66**, 1789 (1994).

[Rob00] J. Robertson, Thins Solid Films **383**, 81 (2000).

[Rob02] J. Robertson, Reports: A Review Journal R **37**, 129 (2002).

[Rod01] S. E. Rodil, A. C. Ferrai, J. Robertson, and W. I. Milne, J. Appl. Phys. **89**, 5425 (2001).

[Rod04] S. E. Rodil, and S. Muhl, Diam. Relat. Mater. **13**, 1521 (2004).

[Rot87] T. H. Roth and K. H. Kloos, Thin Solid Films **153**, 123 (1987).

[Sae94] K. L. Saenger, *Pulsed Laser Deposition of Thin Films*, John Wiley & Sons, New York (1994).

[Sav92] N. Savvides, and T. J. Bell, Appy. Phys. **72**, 2791 (1992).

[Saw99] T. Sawa, Y. Akiyama, and K. Tanaka, J. Mater. Res. **14**, 2228 (1999).

[Sch96] J. Schwan, S. Ulrish, V. Batori, H. Ehrhardt, and S. R. P. Silva, J. Appl. Phys. **80**, 440 (1996).

[Seb98] T. Sebald and R. Kaltofen, Surf. Coat. Tehcnol. **98**, 1280 (1998).

[Sie98] M. P. Siegal, J. C. Barbour, P. N. Provencio, D. R. Tallant, and T. A. Friedmann, Appl. Phys. Lett. **73**, 759 (1998).

[Sie00] M. P. Siegal, D. R. Tallant, P. N. Provencio, L. L. Overmyer, R. L. Simpson, and L. J. Martinez-Miranda, Appl. Phys. Lett. **76**, 3052 (2000).

[Sil97] S. R. P. Silva and G. A. J. Amaratunga, Appl. Phys. Lett. **71**, 1477 (1997).

[Sil02] S. R. P. Silva, J. D. Carey, R. U. A. Khan, and E. G. Gerstner, *Handbook of Thin Film Materials*, Academic Press, New York (2002).

[Sjo96a] H. Sjostrom, L. Hultman, J. E. Sundgren, S. V. Hainsworth, T. F. Page, and G. S. A. M. Theunissen, J. Vac. Sci. Technol. A **14(1)**, 56 (1996).

[Sjo96b] H. Sjostrom, W. Lanford, B. Hjorvarson, K. Xing, and J. E. Sundgren, J. Mater. Res. **11**, 981 (1996).

[Smi01] S. M. Smith, S. A. Voight, H. Tompkins, A. Hooper, and J. Vella, Thin Solid Films **398-399**, 163 (2001).

[Spa97] C. Spaeth, M. Kuhn, and F. Richter, Diam. Relat. Mater. **6**, 626 (1997).

[Spe76] E. G. Spencer, P. H. Schmidt, D. C. Joy and F. J. Sansalone, Appl. Phys. Lett. **29**, 118 (1976).

[Sul01] J. P. Sullivan, and T. Friedmann, Mater. Res. Soc. Bull., May (2001).

[Tab99] M. Tabbal, P. Merel, M. Chaker, M. A. El Khakani, E. G. Herbert, B. N. Lucas, and M. E. O'Hern, J. Appl. Phys. **85**, 3860 (1999).

[Tak97] Y. Taki, T. Kitagawa, and O. Takai, Thin Solid Films **304**, 183 (1997).

[Tam90] M. A. Tamor, and C. H. Wu, J. Appl. Phys. **67**, 1007 (1990).

[Tam94] M. A. Tamor, and W. C. Vassell, J. Appl. Phys. **76(6)**, 3823 (1994).

[Tam95] M. A. Tamor, Mater. Res. Soc. Symp. Proc. **383**, 423 (1995).

[Tan98] Y. Tani, and E. Kamijo, Appl. Phys. Lett. **73**, 1652 (1998).

[Tay99] B. K. Tay, X. Shi, and H. S. Tan, Surf. Interface Anal. 28, **231** (1999)

[Tet96] D. M. Teter, and R. J. Hernley, Science **271**, 53 (1996).

[The04] M. Therasse, and M. Benlahsen, Solid State Comm. **129**, 139 (2004).

[Tsu99] T. Y. Tsui, J. Vlassak, and W. D. Nix, J. Mater. Res. **14**, 2196 (1999).

[Tui70] F. Tuinstra, and J. L. Koening, J. Chem. Phys. **53**, 1126 (1970).

[Ugo90] D. Ugolini, J. Eitle, and P. Oelhafen, Vacuum **41**, 1374 (1990).

[Voe96] A. A. Voevodin, and M. S. Donley, Surf. Coat. Technol. **82**, 199 (1996).

[Wei82] C. Weissmantel, Thin Solid Films **92**, 55 (1982).

[Wei96] M. Weiler, S. Sattel, T. Giessen, K. Jung, H. Ehrhardt, V. S. Veerasamy, and J. Robertson, Phys. Rev. B **53**, 1594 (1996).

[Wei98] M. Weiler, K. Lang, and J. Robertson, Appl. Phys. Lett. **72**, 1314 (1998).

[Wei99] Q. Wei, A. K. Sharma, and J. Narayan, Composites B **30**, 675 (1999).

[Wie01] A. Wieness, M. Neuhauser, and H. H. Schneider, Diam. Relat. Mater. **10(3-7)**, 1024 (2001).

[Woo95] P. Wood, T. Wydeven, and O. Tsuji, Thin Solid Films **258**, 151 (1995).

[Xu98] S. Xu, L. K. Cheah, and B. K. Tay, Thin Solid Films **312**, 160 (1998).

[Yam98] K. Yamamoto, Y. Koga, S. Fujiwara, F. Kokai, and R. B. Heimann, Appl. Phys. **A66**, 115 (1998).

[Yos89] M. Yoshikawa, Mater. Sci. Forum **52-53**, 365 (1989)

[Zha01] J. P. Zhao, Z. Y. Chen, T. Yano, T. Ooie, and M. Yoneda, J. Appl. Phys. **89(3)**, 1580 (2001).

[Zha02] W. Zhang, A. Tanaka, and Y. Koga, Thin Solid Films **416**, 145 (2002).

BIOGRAPHICAL SKETCH

Sang Hyun Yoon was born on March 20, 1973, in Seoul, Korea. He spent most of his youth in Seoul, except when he spent parts of his 5th and 6th grades of elementary school life in California, U.S. After finishing one year in the U.S., he and his family went back to Seoul, Korea. He graduated from Kaepo High School in February, 1992. After that, he went to Hanyang University, in Seoul. He graduated in February, 1997, with a Bachelor of Science in metallurgical engineering. He continued his Master of Science program in the Department of Advanced Materials, Hanyang University. After receiving this M.S. degree, he had interest in more advanced research and decided to come to U.S. for further study. He enrolled in the Department of Materials Science and Engineering at the University of Florida in the fall of 1999 to pursue Ph.D work in the area of electronic materials.

I certify that I have read this study and that in my opinion it conforms to acceptable standards of scholarly presentation and is fully adequate, in scope and quality, as a dissertation for the degree of Doctor of Philosophy.

Rajiv K. Singh, Chairman
Professor of Materials Science and Engineering

I certify that I have read this study and that in my opinion it conforms to acceptable standards of scholarly presentation and is fully adequate, in scope and quality, as a dissertation for the degree of Doctor of Philosophy.

Stephen J. Pearton
Professor of Materials Science and Engineering

I certify that I have read this study and that in my opinion it conforms to acceptable standards of scholarly presentation and is fully adequate, in scope and quality, as a dissertation for the degree of Doctor of Philosophy.

Cammy Abernathy
Professor of Materials Science and Engineering

I certify that I have read this study and that in my opinion it conforms to acceptable standards of scholarly presentation and is fully adequate, in scope and quality, as a dissertation for the degree of Doctor of Philosophy.

Wolfgang Sigmund
Associate Professor of Materials Science and Engineering

I certify that I have read this study and that in my opinion it conforms to acceptable standards of scholarly presentation and is fully adequate, in scope and quality, as a dissertation for the degree of Doctor of Philosophy.

Arthur F. Hebard
Professor of Physics

This dissertation was submitted to the Graduate Faculty of the College of Engineering and to the Graduate School and was accepted as partial fulfillment of the requirements for the degree of Doctor of Philosophy.

December 2004

Pramod Khargonekar

Pramod P. Khargonekar
Dean, College of Engineering

Kenneth Gerhardt
Interim Dean, Graduate School